

ARMY RESEARCH LABORATORY



**An Assessment of Peridynamics for Pre and Post Failure
Deformation**

by Richard Becker and Richard J. Lucas

ARL-TR-5811

November 2011

Report Documentation Page

Form Approved
OMB No. 0704-0188

Public reporting burden for the collection of information is estimated to average 1 hour per response, including the time for reviewing instructions, searching existing data sources, gathering and maintaining the data needed, and completing and reviewing the collection of information. Send comments regarding this burden estimate or any other aspect of this collection of information, including suggestions for reducing this burden, to Washington Headquarters Services, Directorate for Information Operations and Reports, 1215 Jefferson Davis Highway, Suite 1204, Arlington VA 22202-4302. Respondents should be aware that notwithstanding any other provision of law, no person shall be subject to a penalty for failing to comply with a collection of information if it does not display a currently valid OMB control number.

1. REPORT DATE NOV 2011	2. REPORT TYPE	3. DATES COVERED 00-00-2011 to 00-00-2011			
4. TITLE AND SUBTITLE An Assessment Of Peridynamics For Pre And Post Failure Deformation		5a. CONTRACT NUMBER			
		5b. GRANT NUMBER			
		5c. PROGRAM ELEMENT NUMBER			
6. AUTHOR(S)		5d. PROJECT NUMBER			
		5e. TASK NUMBER			
		5f. WORK UNIT NUMBER			
7. PERFORMING ORGANIZATION NAME(S) AND ADDRESS(ES) U.S. Army Research Laboratory,ATTN: RDRL-WMP-B,Aberdeen Proving Ground,MD,21005		8. PERFORMING ORGANIZATION REPORT NUMBER			
9. SPONSORING/MONITORING AGENCY NAME(S) AND ADDRESS(ES)		10. SPONSOR/MONITOR'S ACRONYM(S)			
		11. SPONSOR/MONITOR'S REPORT NUMBER(S)			
12. DISTRIBUTION/AVAILABILITY STATEMENT Approved for public release; distribution unlimited					
13. SUPPLEMENTARY NOTES					
14. ABSTRACT					
15. SUBJECT TERMS					
16. SECURITY CLASSIFICATION OF:			17. LIMITATION OF ABSTRACT	18. NUMBER OF PAGES	19a. NAME OF RESPONSIBLE PERSON
a. REPORT unclassified	b. ABSTRACT unclassified	c. THIS PAGE unclassified	Same as Report (SAR)	44	

NOTICES

Disclaimers

The findings in this report are not to be construed as an official Department of the Army position unless so designated by other authorized documents.

Citation of manufacturer's or trade names does not constitute an official endorsement or approval of the use thereof.

Destroy this report when it is no longer needed. Do not return it to the originator.

Army Research Laboratory

Aberdeen Proving Ground, MD 21005

ARL-TR-5811

November 2011

An Assessment of Peridynamics for Pre and Post Failure Deformation

Richard Becker

Weapons and Materials Research Directorate, ARL

Richard J. Lucas

University of Mississippi, Oxford, MS 38655

REPORT DOCUMENTATION PAGE

Form Approved
OMB No. 0704-0188

Public reporting burden for this collection of information is estimated to average 1 hour per response, including the time for reviewing instructions, searching existing data sources, gathering and maintaining the data needed, and completing and reviewing the collection information. Send comments regarding this burden estimate or any other aspect of this collection of information, including suggestions for reducing the burden, to Department of Defense, Washington Headquarters Services, Directorate for Information Operations and Reports (0704-0188), 1215 Jefferson Davis Highway, Suite 1204, Arlington, VA 22202-4302. Respondents should be aware that notwithstanding any other provision of law, no person shall be subject to any penalty for failing to comply with a collection of information if it does not display a currently valid OMB control number.

PLEASE DO NOT RETURN YOUR FORM TO THE ABOVE ADDRESS.

1. REPORT DATE (DD-MM-YYYY) November 2011		2. REPORT TYPE Final		3. DATES COVERED (From - To)	
4. TITLE AND SUBTITLE An Assessment of Peridynamics for Pre and Post Failure Deformation				5a. CONTRACT NUMBER	
				5b. GRANT NUMBER	
				5c. PROGRAM ELEMENT NUMBER	
6. AUTHOR(S) Richard Becker and Richard J. Lucas				5d. PROJECT NUMBER	
				5e. TASK NUMBER	
				5f. WORK UNIT NUMBER	
7. PERFORMING ORGANIZATION NAME(S) AND ADDRESS(ES) U.S. Army Research Laboratory ATTN: RDRL-WMP-B Aberdeen Proving Ground, MD 21005				8. PERFORMING ORGANIZATION REPORT NUMBER ARL-TR-5811	
9. SPONSORING/MONITORING AGENCY NAME(S) AND ADDRESS(ES)				10. SPONSOR/MONITOR'S ACRONYM(S)	
				11. SPONSOR/MONITOR'S REPORT NUMBER(S)	
12. DISTRIBUTION/AVAILABILITY STATEMENT Approved for public release; distribution unlimited.					
13. SUPPLEMENTARY NOTES					
14. ABSTRACT The peridynamics method was examined in the context of deformation conditions commonly observed before and after dynamic material failure by using a combination of full simulations, targeted numerical techniques, and analytic solutions. The results show numerical dispersion and boundary condition artifacts expected with nonlocal methods, anomalous volume-shear coupling related to the numerical grid, and limitations of the current material model implementations for large strain and impact simulations. Implications of these observations and potential modifications are discussed. Differences and similarities between peridynamics and conventional finite element formulations are also explored.					
15. SUBJECT TERMS Peridynamics, nonlocal, emu, kraken					
16. SECURITY CLASSIFICATION OF:			17. LIMITATION OF ABSTRACT UU	18. NUMBER OF PAGES 44	19a. NAME OF RESPONSIBLE PERSON Richard Becker
a. REPORT Unclassified	b. ABSTRACT Unclassified	c. THIS PAGE Unclassified			19b. TELEPHONE NUMBER (Include area code) (410) 278-7980

Contents

List of Figures	v
Acknowledgments	vii
1. Introduction	1
2. Peridynamics Formulation	1
2.1 Micro-elastic and Micro-plastic Models	2
2.2 State-based Model	2
2.2.1 Kinematics.....	3
2.2.2 Weighting of Distant Nodes	5
2.2.3 Stress and Nodal Forces	5
2.2.4 Failure Modeling	6
3. Numerical Simulation Results	6
3.1 Micro-elastic and Micro-plastic Models	7
3.1.1 1D Elastic Wave Propagation.....	7
3.1.2 1D Elastic Wave Propagation on a Sheared Grid.....	9
3.1.3 1D Plastic Wave Propagation.....	10
3.1.4 Post impact Response.....	10
3.2 State-based Constitutive Model.....	11
3.2.1 1D Elastic Wave Propagation.....	11
3.2.2 1D Plastic Wave Propagation.....	13
3.2.3 Sheared Grid.....	14
3.2.4 Further Coupling Effects with Nonuniform Grid.....	14
3.2.5 Impact with a Spherical Projectile.....	17
4. Kinematics of the State-based Formulation	19
4.1 Analytic Solutions	19
4.1.1 Normal impact with a Shifted Grid	19
4.1.2 Point-wise Solution on Irregular Grid	21
4.1.3 Horizon Effect and Discretization Error	22

4.2	Numerical Evaluation.....	23
4.2.1	Volume-shear Coupling	23
4.2.2	Horizon Effects in a Collapsing Cylinder	25
5.	Discussion	27
6.	Conclusions and Recommendations	30
7.	References	32
	Distribution List	33

List of Figures

Figure 1. Node numbering for example in equations 7 and 8.....	4
Figure 2. Longitudinal (a) and transverse (b) particle velocities at the indicated positions for the micro-elastic material with a horizon of 0.1574 mm, 3.015 times the grid spacing. Results for (a) and (b) are for distinct calculations where a longitudinal or transverse velocity, respectively, was imposed on the surface.	8
Figure 3. Longitudinal particle velocities (a) at the indicated positions for the micro-elastic material with a horizon of 0.071 mm, 1.42 times the grid spacing. Times (b) at which nodes achieved velocities of 1 mm/ms and 9 mm/ms for the horizon values indicated in the legend. The calculated wave speeds are given in the legend.	8
Figure 4. Sheared grid used to assess the volume-shear coupling response indicated in figure 5b.....	9
Figure 5. Longitudinal (a) and transverse (b) particle velocities from a single 1D longitudinal wave calculation with a sheared grid using micro-elastic material. The transverse velocity should be zero.	9
Figure 6. Longitudinal (a) and transverse (b) particle velocities at the indicated positions for the micro-elastic material with a stress cap of 80 MPa. Results for (a) and (b) are for distinct calculations where a longitudinal or transverse velocity, respectively, was imposed on the surface. The persistently lower velocity of the interior nodes in a) indicates a continuous volume decrease.	10
Figure 7. Dense, rigid sphere impacting a brittle material: (a) initial configuration and (b) dilatation after 0.012 ms.....	11
Figure 8. Longitudinal particle velocities obtained from an elastic state-based model (a) without and (b) with viscous drag and hourglass control.....	12
Figure 9. Calculation shown in figure 8b repeated with a smaller time step to illustrate the dissipative influence of the drag algorithm. The thin dashed lines are the curves from figure 8b.....	13
Figure 10. Longitudinal particle velocities for the state-based model where the yield strength is set low to allow plastic deformation.....	14
Figure 11. Transverse particle velocity for simulations using a sheared grid. Results are shown for calculation (a) without and (b) with the drag algorithm.	14
Figure 12. Simulated wave propagation through a spatially graded mesh. The plots show (a) longitudinal velocity (m/s), (b) transverse velocity (m/s), (c) longitudinal-transverse shear stress (MPa), and (d) longitudinal stress (MPa).	15
Figure 13. Horizontal velocity field (m/s) creating two simple shear regions. The solid color regions at the top, center and bottom are nodes where the velocity is imposed.	17
Figure 14. The (a) out of plane stress (MPa) and (b) dilatation resulting from imposed simple shear boundary conditions on the graded mesh.	17
Figure 15. Dilatation plot for a dense, rigid sphere impacting a ductile target. The disordered	

nodes and color levels combined with an apparent densification suggest a breakdown of the calculation. The initial configuration is shown in figure 7a.	18
Figure 16. Dilatation plot for a dense, rigid sphere impacting a brittle target. The tight node packing suggests that the hydrodynamic response is being controlled by the short-range interaction force rather than the constitutive response.	19
Figure 17. Shifted 2D grid used to investigate volume-shear coupling.....	20
Figure 18. Grid with single point shifted to create a zero shear error at a specific node.....	21
Figure 19. Grid configurations illustrating volume-shear coupling. (a), (c) and (e) show the volume change imposed on the grid. Plots (b), (d) and (f) illustrate the corresponding shear induced by the volume change.	24
Figure 20. Calculated volume change resulting from nodal displacements corresponding to an isochoric deformation field. The horizon for the plots is: (a) 1.015, (b) 1.5, (c) 2.015, (d) 2.3, (e) 3.015, and (f) 3.2 times the grid spacing. The color levels are the same for each plot.	26

Acknowledgments

Richard Lucas was supported by an appointment through the Oak Ridge Institute for Science and Education, proposal 1120-1120-99.

INTENTIONALLY LEFT BLANK.

1. Introduction

There are a wide variety of computational tools available for analysis and design of munitions and armor. While simulations of high-rate dynamic loading have predominantly used finite element and hydro codes, emerging methods also receive attention. One relatively new approach is peridynamics (1–3). Initially proposed at Sandia National Laboratories (1), it was developed with fracture simulations in mind. The concept is that integrating over pair-wise interactions among material points ameliorates some of the difficulties encountered when formulating fracture problems with continuum-based methods that rely on continuous fields to evaluate gradients. Most of the use of peridynamics to date has been for studies of fracture and fragmentation (4–6). As the peridynamics codes now include plasticity (2, 7) and are becoming more widely available (8, 9), there is a desire to apply them quantitatively and to a broader class of problems.

As with many tools, there will be some areas where peridynamics will be advantageous, and there may be other areas where it is not the most appropriate method. The intent of this report is to begin defining the role for peridynamics by providing an assessment for high-rate deformation simulations, including large strain deformations that often precede fracture and material flow accompanying ballistic impact.

The report will begin with an overview of the peridynamics equations; first the micro-elastic and micro-plastic models will be outlined, and then the newer state-based formulation will be presented along with a comparison to traditional finite elements. Numerical examples will be presented to assess peridynamics results in deformation scenarios that typically accompany fracture or ballistic impact. The origins of any unexpected behaviors are explored through parameter studies and analysis. Recommendations will be made regarding the range of applicability of peridynamics for high-rate deformation problems.

2. Peridynamics Formulation

The initial formulation of peridynamics (1) was focused on integration of pair-wise particle interactions over some domain surrounding a material point. This provides a convenient framework for elastic models. However, the pair-wise model construct is not sufficiently flexible to incorporate traditional nonlinear constitutive relations, nor is it amenable to representing field relations that are typically expressed as differential equations. The peridynamics framework was subsequently extended to a state-based approach (2, 7) to facilitate use of common nonlinear constitutive models and more general field equations. Both the micro-elastic and the state-based formulations are discussed.

2.1 Micro-elastic and Micro-plastic Models

Peridynamics solves the traditional momentum equation at material points within a body.

$$\mathbf{f}(\mathbf{x}, t) + \mathbf{b}(\mathbf{x}, t) = \rho \ddot{\mathbf{u}} \quad (1)$$

Here t is time, \mathbf{x} are the coordinates of the point, \mathbf{u} is the displacement of the point, \mathbf{f} is the force acting on the point by the surroundings, \mathbf{b} is the body force, and ρ is the density. The double dot denotes the second time derivative. The force is obtained from a function of pair-wise differences in displacements and coordinates integrated over the region \mathfrak{R} surrounding the point.

$$\mathbf{f}(\mathbf{x}, t) = \int_{\mathfrak{R}} \mathfrak{F}[\mathbf{u}(\mathbf{x}', t) - \mathbf{u}(\mathbf{x}, t), \mathbf{x}' - \mathbf{x}] dV_{x'} \quad (2)$$

The prime denotes the other points in the region connected to the point of interest. To make the solution tractable, the integration over material points within region \mathfrak{R} is replaced by a summation over more widely spaced nodes within a radius called the horizon. The horizon is set to 3.015 times the grid spacing by default in the peridynamics codes EMU (8) and KRAKEN (9).

Failure occurs by progressive fracturing of individual links as the local strain limit is exceeded. The failure criterion is similar to that available in many finite element codes, but the progressive failure aspect is less common. Once a link has failed, the connection between the nodes is lost.

The micro-elastic and micro-plastic models both provide a linear force-displacement relationship between nodes, with a cap on the peak force (yield) and a critical force to failure. The response in unloading is different for the two treatments in that the elastic model unloads along the original path and the plastic model unloads with the elastic slope.

The micro-elastic/micro-plastic model is limiting in two respects. There is a single elastic constant, whereas an isotropic elastic continuum material has two. For the micro-elastic and micro-plastic models, the modulus is related to the speed of a longitudinal stress wave and the Poisson's ratio is fixed at 1/4 (I). The Poisson's ratio cannot be varied. The second limitation is that yield applies to the total model behavior. In a traditional elastic-plastic continuum model, the yield affects the deviatoric part of the behavior while the volumetric part remains elastic.

2.2 State-based Model

The state-based peridynamics formulation addresses some of the limitations of the micro-elastic and micro-plastic models. It is useful to begin the state-based peridynamics presentation by giving some of the basic equations in comparison to Lagrangian finite element methods (FE/FEM). Operationally, both peridynamics and Lagrangian FEM have nodes attached to material points that track displacements and velocities. In peridynamics, the strain and stress are also resident on the nodes, and quantities are obtained by integration over other nodes within a given radius called the horizon. There is no explicit mesh. In FEM, elements are constructed with

the nodes as the vertices, and the strain and stress are obtained by integration over the element volumes.

2.2.1 Kinematics

The expressions for the continuum representation of the average deformation gradient in peridynamics over its horizon (7) and the average deformation gradient within a finite element (10) are, respectively

$$\mathbf{F}^{Peri} = \int_{\mathcal{H}} \omega(|\xi|)(\mathbf{Y} \otimes \xi) dV_{\mathbf{x}'} \mathbf{K}^{-1} \quad \text{and} \quad \mathbf{F}^{FE} = \frac{1}{V} \int_V \left(\frac{d\mathbf{x}}{d\mathbf{X}} \right) dV. \quad (3)$$

Both methods involve volume integrals. \mathbf{x} are the coordinates of a material point initially located at \mathbf{X} . The relative position between two material points in the initial configuration is define as $\xi = \mathbf{X}' - \mathbf{X}$, and the relative position in the current configuration is $\mathbf{Y} = \mathbf{x}' - \mathbf{x}$. The volume integration in peridynamics is over all points within the horizon except the focus point, \mathbf{x} . The weight, $\omega(|\xi|)$, is generally equal to one except when bonds are fractured, and the shape tensor is defined as

$$\mathbf{K} = \int_{\mathcal{H}} \omega(|\xi|)(\xi \otimes \xi) dV_{\mathbf{x}'} . \quad (4)$$

Heuristically, for a uniform point spacing in peridynamics, the integrated volumes from equations 3 and 4 cancel, as does a ξ from each. This leaves the sum of the current distances between points divided by the sum of the original distances. This result has the appearance of the definition of a derivative, as it must to produce the deformation gradient. Hence, in a loose sense, the deformation gradient in peridynamics is produced by the definition of a derivative while it is a formal mathematical derivative in the finite element formulation. A crack in the continuum FE formalization is a singularity, while in peridynamics it is a spike that can be made arbitrarily large or small depending on the chosen material point spacing.

This distinction in the integrand singularity becomes academic when considering the numerical implementation of the techniques on a discrete grid of nodes. In discrete form, the deformation gradient for the two methods from equation 3 becomes

$$\mathbf{F}^{Peri} = \sum_{n=1}^K [\omega(|\xi_n|)(\mathbf{Y}_n \otimes \xi_n)V_n] \mathbf{K}^{-1} \quad \mathbf{F}^{FE} = \sum_{n=1}^N \mathbf{x}_n \otimes \mathbf{B}^n . \quad (5)$$

The \mathbf{B}^n in the FE representation, equation 5b, is the standard difference operator. The summation for peridynamics is over the nodes in the horizon, and for finite elements is it over the nodes defining the element. The discrete relative position vector is $\xi_n = \mathbf{X}_n - \mathbf{X}_m$, where \mathbf{X}_m is the initial location of the focus node, and the definitions of \mathbf{Y} and \mathbf{K} follow similarly. Recognizing that \mathbf{K}^{-1} is a constant in equation 5a, it can be taken inside the summation and rewritten as

$$\mathbf{F}^{Peri} = \sum_{n=1}^K [\mathbf{Y}_n \otimes (\boldsymbol{\xi}_n \cdot \mathbf{K}^{-1} \omega(|\boldsymbol{\xi}_n|) V_n)] = \sum_{n=1}^K [(\mathbf{x}_n - \mathbf{x}_m) \otimes \check{\mathbf{B}}^n] , \quad (6)$$

where the $\check{\mathbf{B}}^n$ is a vector of dimension inverse length operating on differences between coordinates.

As an illustration of what is calculated numerically, consider the 2D deformation gradient computed for the center point of a set of nine regularly spaced points, figure 1, with both x -spacing and y -spacing equal to d . For peridynamics the horizon is set at 1.5, which is smaller than typically used, but it facilitates comparison with the FE. The deformation gradient from the FE solution is averaged for the four elements surrounding the center node, which is also not normally done, but it likewise facilitates the comparison.

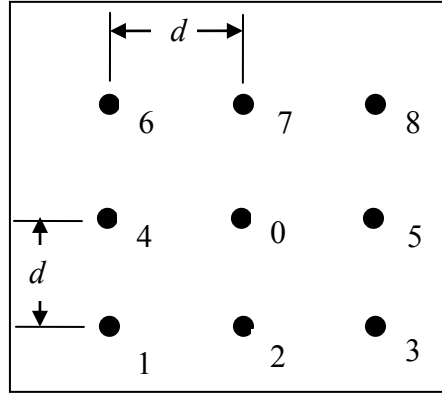


Figure 1. Node numbering for example in equations 7 and 8.

The 2D deformation gradient components computed for the two methods are

$$F_{ij}^{Peri} = \frac{1}{6d} \begin{bmatrix} (-x_1 + x_3 - x_4 + x_5 - x_6 + x_7) & (-x_1 - x_2 - x_3 + x_6 + x_7 + x_8) \\ (-y_1 + y_3 - y_4 + y_5 - y_6 + y_7) & (-y_1 - y_2 - y_3 + y_6 + y_7 + y_8) \end{bmatrix} \quad (7)$$

$$F_{ij}^{FE} = \frac{1}{8d} \begin{bmatrix} (-x_1 + x_3 - 2x_4 + 2x_5 - x_6 + x_7) & (-x_1 - 2x_2 - x_3 + x_6 + 2x_7 + x_8) \\ (-y_1 + y_3 - 2y_4 + 2y_5 - y_6 + y_7) & (-y_1 - 2y_2 - y_3 + y_6 + 2y_7 + y_8) \end{bmatrix} . \quad (8)$$

In this example, the distinction between the two methods is in the weighting of points at the center of the edges of the grid. The operations on the coordinates are otherwise similar in this example.

The number of nodes involved in the summations for peridynamics and FE simulations will be quite different in typical applications, potentially leading to significantly different computational results. The horizon for peridynamics simulations will be larger (the default is 3.015 times the average node spacing), and the weighted sums and differences in 3D could span more than 100 nodes. This makes peridynamics a nonlocal method which has additional consequences for solving the fundamental equations. On the other hand, deformation gradients for uniform strain,

hexahedral finite elements will be computed by weighted sums and differences of eight nodes. It is a local method. The similarity is that both methods use weighted sums of nodal values; they will not necessarily give similar results.

2.2.2 Weighting of Distant Nodes

Peridynamics is a nonlocal method in that the behavior at a material point can be affected by the deformation and stress fields beyond its local vicinity. The weighting function, ω , can be used to control the influence of distance points relative to points in the immediate neighborhood.

However, the current defaults in EMU are to have the weighting factor equal to one for all points within the horizon prior to failure. The user's manual (8) does not indicate a way to change the weighting at this time.

With a weighting factor of one, the structure of peridynamics places a greater weight on nodes near the horizon than on nodes near the focus point. As an example, consider a uniform 1-D grid with spacing, d , subjected to a uniform stretch, λ . The horizon is 3.015 times d . This has initial relative position vector magnitudes, ξ , equal to d for the nodes adjacent to the focus node and equal to $3d$ for nodes near the horizon. The current relative position magnitudes are λd for the adjacent nodes and $3\lambda d$ for the nodes near the horizon. Multiplying these as indicated in equation 3a results in the nodes near the horizon having nine times the weight of the nodes adjacent to the focus point when computing the sums.

2.2.3 Stress and Nodal Forces

State-based peridynamics and FE both use the same momentum equation, equation 1, and similar constitutive models to integrate Cauchy stress given the applied deformation history. Formulas translating the stress to a peridynamics nodal force vector state (7)* and to nodal forces in FE (10) are, respectively

$$\tilde{\mathbf{f}}(\xi_n)^{Peri} = \omega(|\xi_n|) \boldsymbol{\sigma}_m \cdot \mathbf{K}^{-1} \cdot \xi_n V_m \quad \text{and} \quad \mathbf{f}_n^{FE} = \mathbf{B}^n \cdot \boldsymbol{\sigma} V . \quad (9)$$

Similar to equation 6, and using the symmetry of \mathbf{K} , equation 9a can be written in terms of $\tilde{\mathbf{B}}^n$ as

$$\tilde{\mathbf{f}}(\xi_n)^{Peri} = \xi_n \cdot \mathbf{K}^{-1} \cdot \boldsymbol{\sigma}_m \omega(|\xi_n|) V_m = \tilde{\mathbf{B}}^n \cdot \boldsymbol{\sigma}_m . \quad (10)$$

As with the expressions for the deformation gradients, the relations for the forces have similarities. However, there are notable differences in how the individual forces are combined to give the net force on a node. Peridynamics uses a sum of differences between force vector states integrated over the volume.

$$\mathbf{f}(\mathbf{x}_m) = \sum_{n=1}^K [\tilde{\mathbf{f}}(\mathbf{x}_n - \mathbf{x}_m) - \tilde{\mathbf{f}}(\mathbf{x}_m - \mathbf{x}_n)] V_n \quad (11)$$

*The force vector state defined in equation 25 of reference 7 appears to be dimensionally incorrect for a force since \mathbf{K} has dimension of L^{-5} . The presumed missing volume has been included in equation 9 above.

The resulting nodal force involves a difference in stresses among neighboring nodes. These stress differences can be viewed as comprising a gradient in the stress field, which resembles the strong form of the momentum equations. Finite element formulations use a weak form of the momentum equations, and the forces from equation 9b are simply summed at the nodes.

2.2.4 Failure Modeling

Failure for the state-based materials in the peridynamics code EMU is triggered when a critical bond strain is attained. The bonds between nodes are broken individually as they reach the failure criterion, resulting in a progressive material failure. FE methods are similar in that connections among the nodes of an element are modified when the element reaches a failure criterion. The connections within an element can be weakened gradually or removed abruptly depending on the failure model used. The gradual failure progression in peridynamics would make fracture propagation less sensitive to numerical discretization than abrupt element failure in FE methods.

After failure, the peridynamic bonds are broken. In tension, the nodes are free to separate without constraint. To prevent unrealistic densification of failed materials in compression, short-range interaction forces are imposed when nodes are closer than some critical distance.

3. Numerical Simulation Results

Peridynamics codes EMU (8) and KRAKEN (9) were obtained from Sandia National Laboratories and installed on the Department of Defense (DoD) high-performance computing platform (HPC), *harold*. Although the parallel executables were built, the simulations were sufficiently small enough that all runs were on a single processor.

The simulations were designed to assess basic dynamic material response that would occur prior to or in combination with fracture. The goal was to examine quantitative aspects of physics that represent basic behavior, rather than features of the solution that would be highly variable and model dependent. Hence, fracture behavior itself is not considered. The simulations were as follows: low velocity 1D wave propagation, inhomogeneous simple shear, and low speed impact with a spherical projectile. Since neither code incorporated artificial viscosities necessary for shock simulations, the loading rates were relatively slow, and oscillatory results are expected.

The use of wave propagation examples is not to focus on wave mechanics, but rather to impose sharp gradients in the deformation field in a configuration where the response is well-understood. There are many more general configurations that would result in steep gradients, such as plugging associated with penetration; but the response in these situations is not understood as well, and errors would be more difficult to quantify.

3.1 Micro-elastic and Micro-plastic Models

The micro-plastic model is the same as the micro-elastic model except for the unloading response, so only the micro-elastic model was evaluated. The material used for the 1D micro-elastic simulations resembles aluminum. The density was 0.0027 g/mm^3 and the longitudinal sound speed was 5750 mm/ms . The yield strength and failure strain were varied as part of the assessment and will be specified for each simulation.

3.1.1 1D Elastic Wave Propagation

Elastic wave propagation was investigated using a body $4 \text{ mm} \times 4 \text{ mm} \times 1 \text{ mm}$ thick and with a regular node spacing 0.05 mm . The horizon was 0.1575 mm , 3.015 times the grid spacing. The yield stress was 1 GPa to inhibit yielding, and the fracture strain was set to 1000 to preclude fracture.

Both longitudinal and shear waves were simulated using KRAKEN (9). A 10 mm/ms longitudinal or transverse velocity was imposed on one $4 \text{ mm} \times 4 \text{ mm}$ face at $t=0$, and the opposite face was stress free. Velocities were recorded at nodes at the surface where the velocity boundary condition was imposed; at depths of 0.30 mm , 0.35 mm , 0.40 mm , 0.45 mm , and 0.50 mm ; and at the free surface. The velocity histories are shown in figure 2a for the longitudinal wave and in figure 2b for the transverse wave. The waves are smooth and well-behaved. The oscillations are expected given the spatial discretization and no artificial viscosity to treat the shock dissipation.

The deformation and forces are smoothed over the nodes within the horizon resulting in a spreading of the wave front. This smoothing was examined by rerunning the longitudinal wave simulation with a horizon of 0.071 mm , 1.42 times the grid spacing. The resulting velocity profiles are shown in figure 3a. Comparing this with figure 2a, it is noted that narrower horizon results in a sharper rise time for the wave front. The nonlocal nature of the peridynamics formulation is responsible for spreading the gradient.

The wave propagation was analyzed quantitatively to obtain measures of the wave speed and the front width. Given the broad wave front width, these quantities will vary based on how they are measured. Using the data in figures 2a and 3a, times are determined when the nodes reach 10% and 90% of the imposed velocity. These data from the five internal nodes are plotted in figure 3b. The free surface nodes were not included because the reflection from the free surface might modify the timings. The slope of the line connecting the two end points of each line is given; this is the wave speed at the particular location.

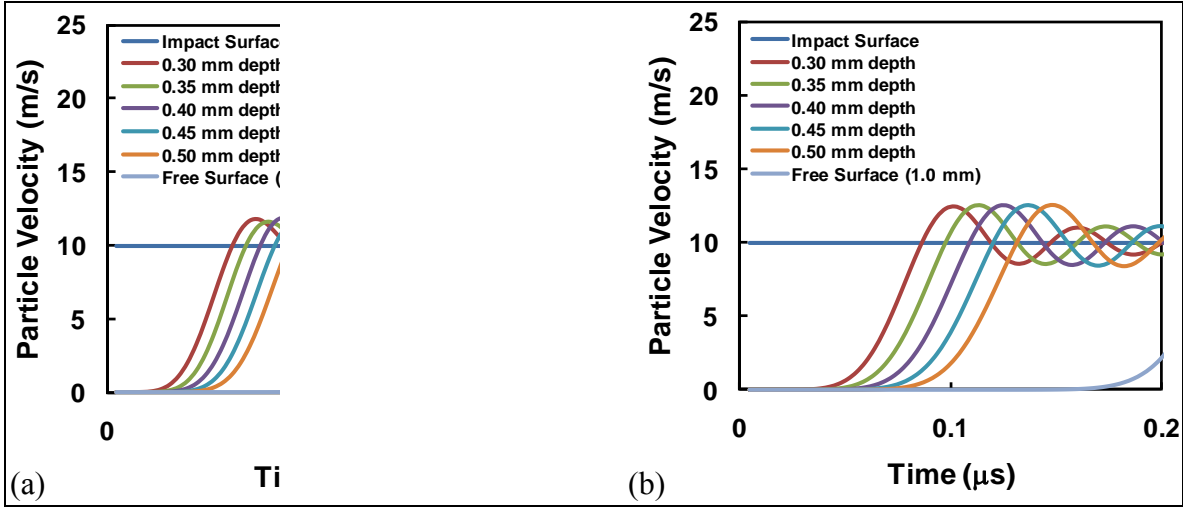


Figure 2. Longitudinal (a) and transverse (b) particle velocities at the indicated positions for the micro-elastic material with a horizon of 0.1574 mm, 3.015 times the grid spacing. Results for (a) and (b) are for distinct calculations where a longitudinal or transverse velocity, respectively, was imposed on the surface.

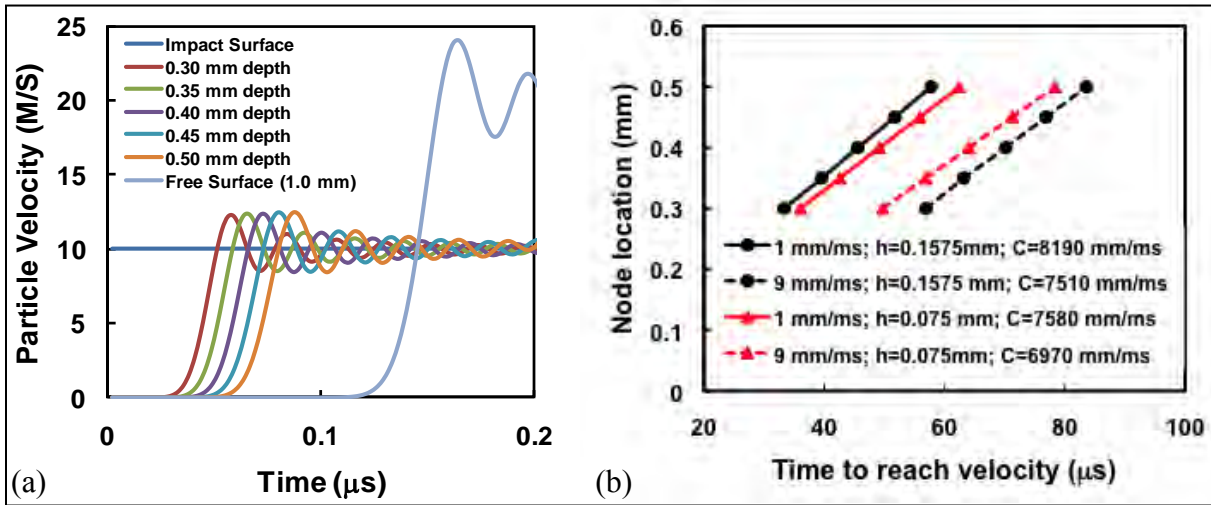


Figure 3. Longitudinal particle velocities (a) at the indicated positions for the micro-elastic material with a horizon of 0.071 mm, 1.42 times the grid spacing. Times (b) at which nodes achieved velocities of 1 mm/ms and 9 mm/ms for the horizon values indicated in the legend. The calculated wave speeds are given in the legend.

Several observations can be made from figure 3b. First, the wave speed is significantly greater than the value placed in the input deck. Second, for both horizon values, the wave speed at the 90% velocity is less than at the 10% velocity. This implies that the wave is broadening as it traverses the sample. Third, using the measured wave speed, the average distance the wave traveled between 10% and 90% velocities is approximately 0.19 mm for the 0.1575 mm horizon and approximately 0.11 mm for the 0.071 mm horizon. These distances indicate the wave front width, which corresponds to roughly four and two node separations, respectively.

3.1.2 1D Elastic Wave Propagation on a Sheared Grid

The elastic wave propagation simulations with the 0.1575 mm horizon were repeated using a grid where each successive plane of nodes in the thickness direction (1 mm direction) was shifted parallel to this plane by 20% of the node spacing. When sectioned, the nodes are the vertices of parallelograms, as shown in figure 4.

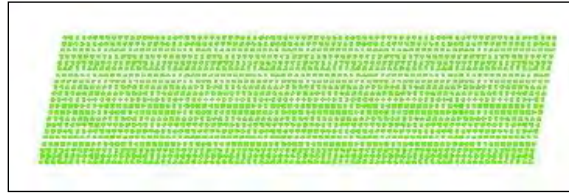


Figure 4. Sheared grid used to assess the volume-shear coupling response indicated in figure 5b.

The results of these sheared grid simulations are shown in figure 5. The longitudinal particle velocities, figure 5a, are similar to that of figure 2a, but the wave arrived at the free surface approximately $0.008 \mu\text{s}$ sooner. Figure 5b shows the node velocities perpendicular to the direction of wave propagation. The peak transverse node velocity is about 2% of the applied velocity. This volume-shear coupling is an anomalous result related to the node distribution within the horizon. If the grid shift is 0 or 0.5 of the node spacing, the configuration is symmetric, and the transverse velocity is zero. This shear will be explored further in section 4.1.1.

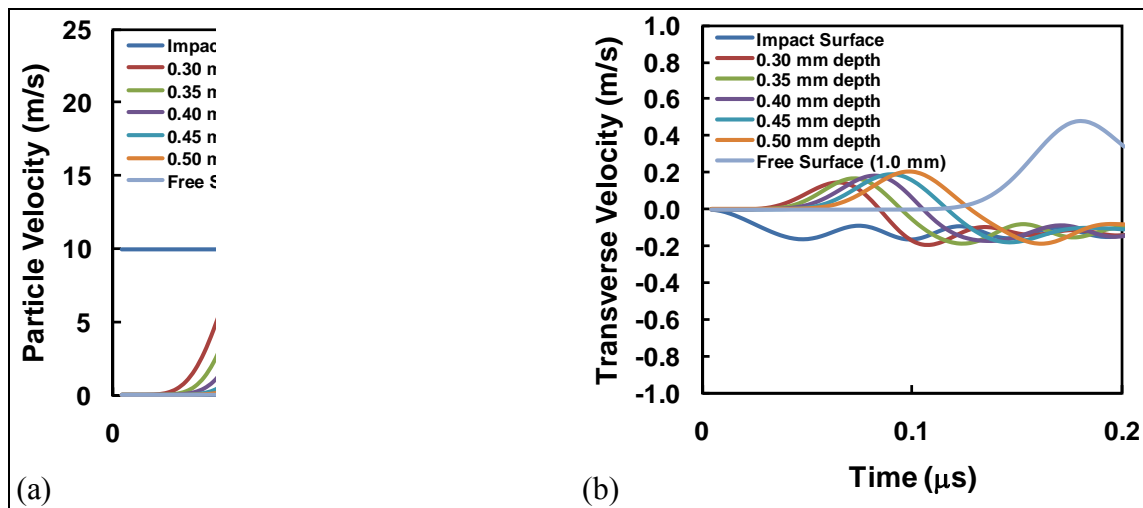


Figure 5. Longitudinal (a) and transverse (b) particle velocities from a single 1D longitudinal wave calculation with a sheared grid using micro-elastic material. The transverse velocity should be zero.

3.1.3 1D Plastic Wave Propagation

The wave propagation simulations of section 3.1.1 were repeated using KRAKEN, with the yield strength lowered to 80 MPa to exercise the cap on the micro-elastic model. All other aspects of the input were identical to those in section 3.1.1.

The resulting node velocity history plots for the applied longitudinal and transverse velocity boundary conditions are shown in figures 6a and 6b, respectively. The nodes interior to the specimen reach a velocity of approximately 4 mm/ms, with little oscillation due to the dissipative nature of the plastic deformation. The velocity of the interior nodes is governed by the stress cap, which limits the driving force for nodal accelerations.

The critical point to note is that the interior velocities only reach 4 mm/ms velocity, while the surface is still moving at 10 mm/ms. In the longitudinal wave simulation, this indicates a continued densification over time. This result is not physically realistic, as the compressive response after yield should be governed by the equation of state. For the shear simulation, the difference between the surface and internal velocities corresponds to strain localization at the surface.

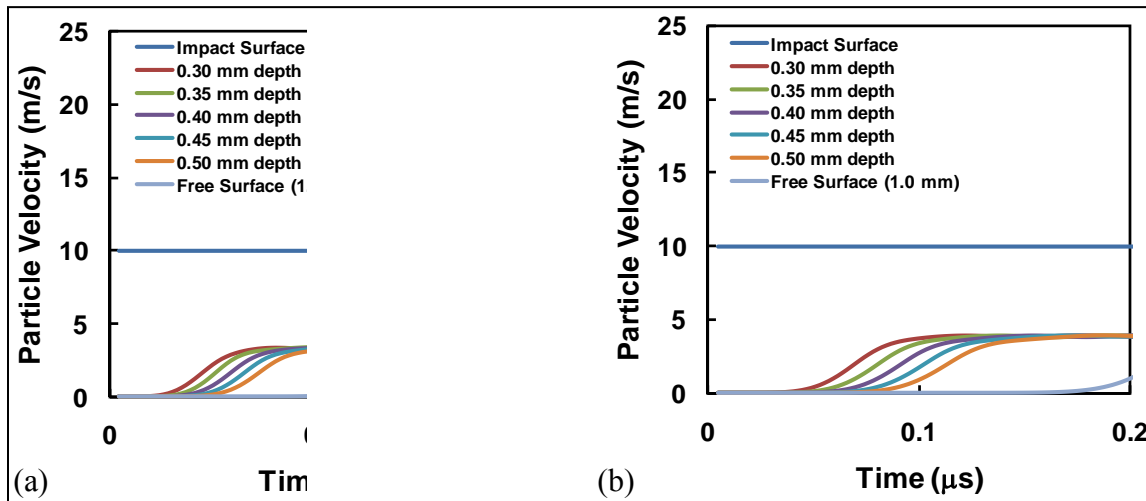


Figure 6. Longitudinal (a) and transverse (b) particle velocities at the indicated positions for the micro-elastic material with a stress cap of 80 MPa. Results for (a) and (b) are for distinct calculations where a longitudinal or transverse velocity, respectively, was imposed on the surface. The persistently lower velocity of the interior nodes in a) indicates a continuous volume decrease.

3.1.4 Post impact Response

The behavior of the micro-elastic model following compressive failure was examined by simulating a sphere impacting a brittle block. A 30 mm square target with a 0.5-mm grid-spacing was impacted by a dense, rigid, 10 mm diameter sphere traveling at 200 mm/ms. The target had a density of 0.0022 g/mm³, a sound speed of 5750 mm/ms, a yield strength of 1300 MPa, and a failure strain of 0.001. The initial configuration is shown in figure 7a.

The configuration 0.012 ms after impact is shown in figure 7b, where the false-color image is of material dilatation. The densification under the projectile at this time is approximately 40%, much greater than would be expected under these impact conditions. The links connecting the nodes are removed after failure, and the material is compressed. It is not possible to enforce volume constraints from an equation of state separately from material failure using the simple micro-elastic model, and the post-impact densification is regulated only by the short-range interaction forces. To produce an acceptable response in compression, the short-range interactions would have to be modified to correspond to an equation of state. This type of post-fracture response is not an issue in most tensile failures where the fractured interfaces do not interact.

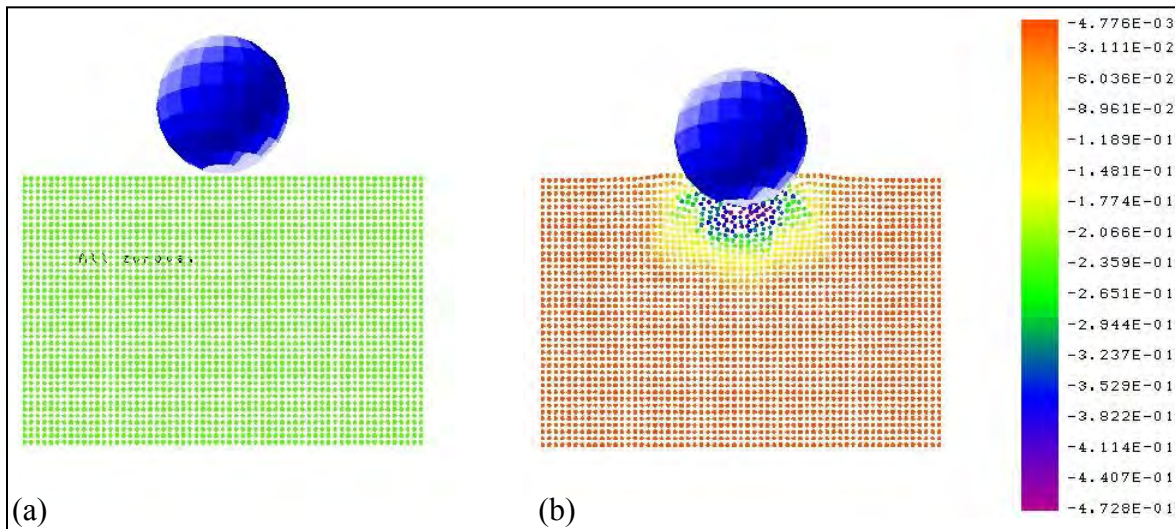


Figure 7. Dense, rigid sphere impacting a brittle material: (a) initial configuration and (b) dilatation after 0.012 ms.

3.2 State-based Constitutive Model

The state-based models remove many of the limitations of the micro-elastic and micro-plastic models by providing a connection to traditional continuum material constitutive models. Several of the assessment simulations presented in the previous section are repeated with the state-based models in EMU. The properties for the wave problems are again chosen to resemble aluminum with a density of 0.0027g/mm^3 , Young's modulus of 70 GPa, and Poisson's ratio of 0.3. The yield strength was set arbitrarily to provide either elastic or plastic deformation.

3.2.1 1D Elastic Wave Propagation

Elastic 1D wave propagation analyses on 1 mm thick specimens were run in EMU using a 1 GPa yield strength and imposing a 10 mm/ms velocity. The response with the state-based models is sensitive to the averaging within the horizon near the boundary (11), so the velocity boundary condition was applied to all nodes within the horizon of the surface.

Plots of longitudinal particle velocity at several locations through the sample thickness are shown in figure 8a. It can be seen that the wave propagation is not steady through the thickness.

The developers recommended (11) adding drag terms to control zero-energy modes and reduce the noise. The drag algorithm replaces the velocity of a node with a weighted sum of the original velocity and the average velocity of all the nodes in the family. Since there is no damage in these problems, the adjusted nodal velocity is given by

$$\tilde{V}_n = (1 - D)V_n + D \frac{1}{K} \sum_{m=1}^K v_m, \quad (12)$$

where the drag coefficient, D , has been set to 0.05. Application of the drag algorithm reduced the variability in nodal velocity and produced a reasonably steady velocity profile for the nodes beyond the center (figure 8b). However, the drag algorithm is a smoothing technique and does not specifically target hourglass models. It also alters aspects of the solution not related to hourglassing.

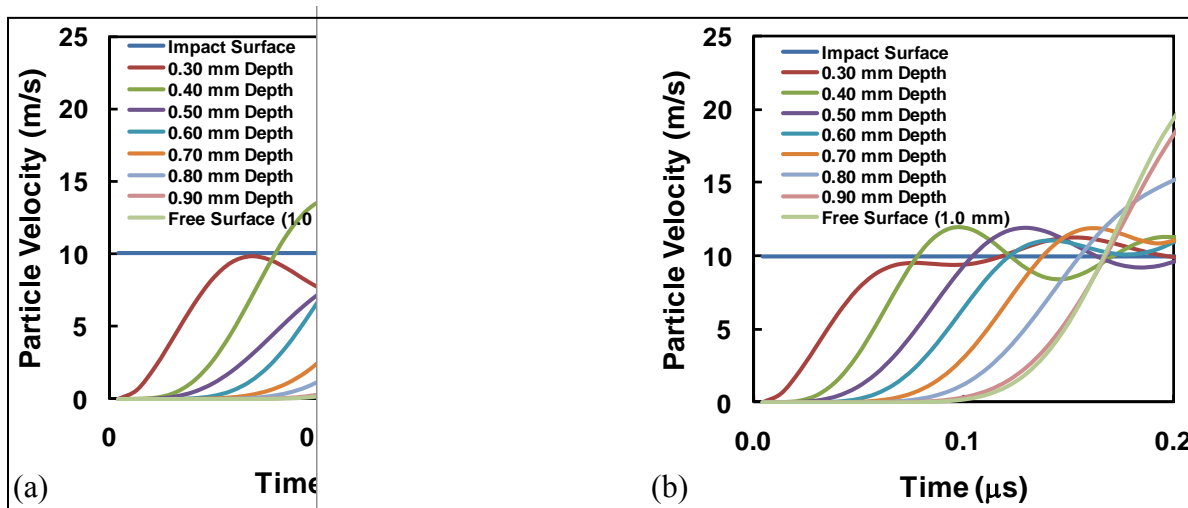


Figure 8. Longitudinal particle velocities obtained from an elastic state-based model (a) without and (b) with viscous drag and hourglass control.

It is notable that the nodes at 0.9 mm and the free surface have nearly the same velocity-time history. Since this is the same with and without the drag algorithm, it is likely due to a combination of the averaging within the horizon, a nonlocal effect, and the long time period for diffuse wave reflections from the free surface.

Wave velocity is more difficult to discern than in section 3.1.1, but it is approximately 8000 mm/ms when the particle velocity is 0.1 mm/ms, and approximately 5400 mm/ms when the particle velocity is 0.9 mm/ms. The latter roughly corresponds to the expected longitudinal wave velocity for the material parameters provided. As with the micro-elastic model, the higher wave speed at the lower particle velocity indicates that the wave is spreading over time.

The drag algorithm in equation 12 averages velocities on every time step, resulting in significant smoothing of the solution. Since it is applied once per time step, the same calculation run with a smaller time step would have many more smoothing operations applied. This time step effect is illustrated by comparing figure 8b, which was run in 23 time steps, to the same input run with 179 time steps, shown in figure 9. The results from figure 8b are included as thin dashed lines in figure 9. It is evident that the oscillations are damped further, and that the rise time for the waves has been lengthened by increasing the number of time steps.

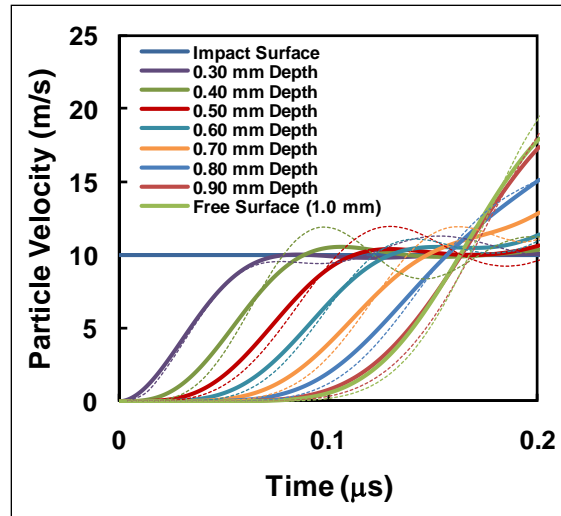


Figure 9. Calculation shown in figure 8b repeated with a smaller time step to illustrate the dissipative influence of the drag algorithm. The thin dashed lines are the curves from figure 8b.

3.2.2 1D Plastic Wave Propagation

Plastic 1D wave propagation analyses on 1-mm thick specimens were run using the state-based model in EMU with a 50-MPa yield strength and imposing a 10-mm/ms velocity. As with the elastic solution, the velocity boundary conditions were imposed on several layers of nodes near the surface, and drag and hourglass algorithms were used to smooth the velocity fields.

Particle velocities at several locations through the sample thickness are shown in figure 10. Compared to the elastic solution, the rise time for the wave is considerably longer. The kink evident in the curves 0.5 mm and deeper is associated with the elastic-plastic transition. However, the response is smoothed considerably since the velocities are averaged over the horizon, and the stresses are effectively averaged over two horizon distances surrounding a node. This is in addition to the smoothing caused by the drag algorithm. The node spacing would have to be significantly finer to capture the nearly vertical rise and plateau normally associated with the Hugoniot elastic limit.

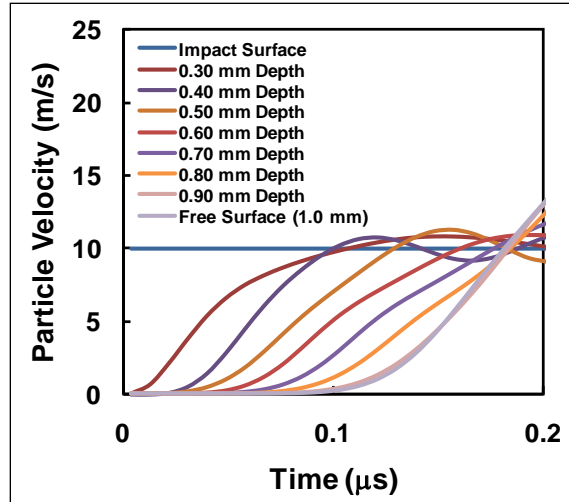


Figure 10. Longitudinal particle velocities for the state-based model where the yield strength is set low to allow plastic deformation.

3.2.3 Sheared Grid

The state-based model with a 50-MPa yield strength was run with a 10-mm/ms impact velocity using the sheared grid in figure 4 to determine if the volume-shear coupling was also present with the state-based models. Results are shown in figure 11 for simulations without and with the drag algorithm. It is evident that the incongruous volume-shear coupling is still present, but the drag algorithm imposes sufficient constraint to reduce the shear error by an order of magnitude.

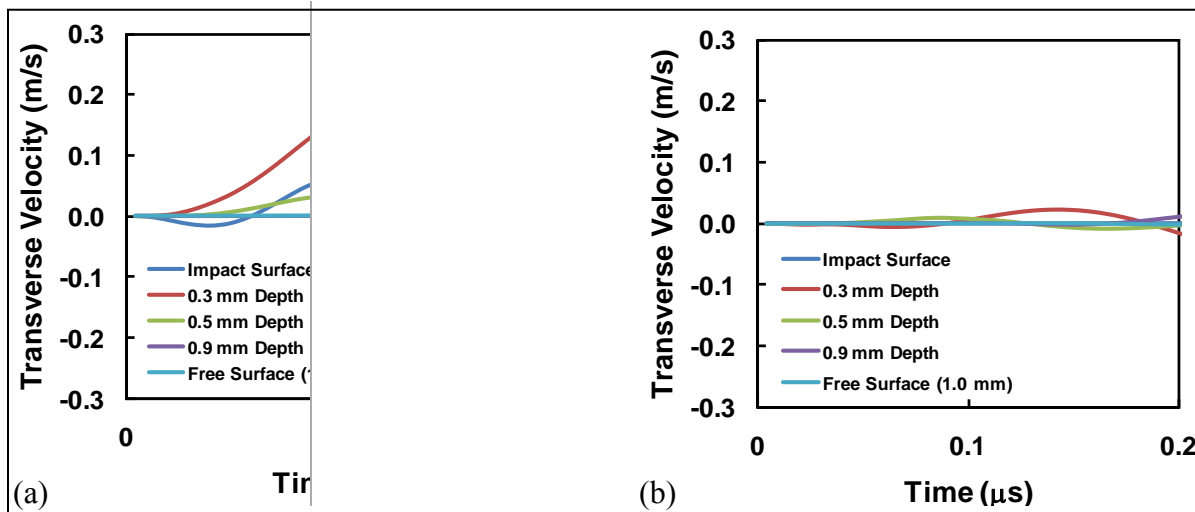


Figure 11. Transverse particle velocity for simulations using a sheared grid. Results are shown for calculation (a) without and (b) with the drag algorithm.

3.2.4 Further Coupling Effects with Nonuniform Grid

The effects of grid nonuniformity were further examined by propagating a wave through a spatially graded grid. A section through the center plane of the grid is depicted in figure 12. The

grid spacing is a uniform 0.05 mm in the vertical direction and in the depth direction. In the transverse direction, the mesh is uniformly spaced at 0.0294 mm for 1 mm on the left, followed by 2 mm of graded mesh where the node spacing increases by 2.5% for successive columns of nodes. The last 1 mm is also a uniform grid with a spacing of 0.0833 mm. Wave propagation and shear calculations were run with this grid.

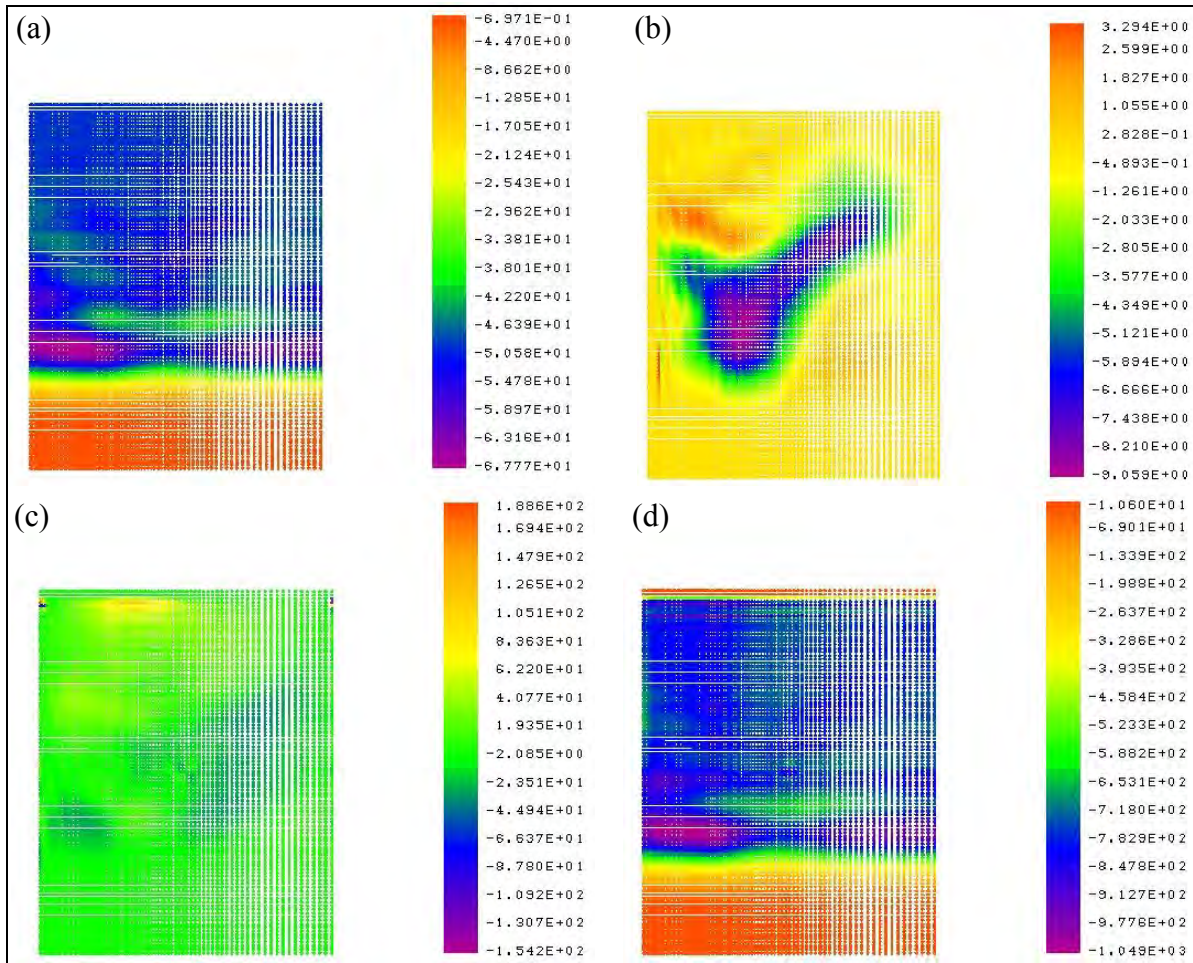


Figure 12. Simulated wave propagation through a spatially graded mesh. The plots show (a) longitudinal velocity (m/s), (b) transverse velocity (m/s), (c) longitudinal-transverse shear stress (MPa), and (d) longitudinal stress (MPa).

The first simulation is a 50-mm/ms velocity imposed on the upper surface, resulting in a wave propagating vertically downward through the mesh. Symmetry boundary conditions are applied over 0.15 mm strips of material in the out of plane and in the lateral directions to suppress edge effects. Results are shown in figure 12. The longitudinal velocity and stress—figures 12a and 12d, respectively—show the location of the wave front. They also show that the solution is significantly different in the center region of the specimen, where the grid spacing is graded, than on either end where the grid spacing is uniform.

A transverse velocity is induced by the mesh gradation, shown in figure 12b. The magnitude of the transverse velocity is roughly 15% of the applied velocity, which is a very large volume-shear coupling effect. This introduces a correspondingly large shear stress, which is captured in figure 12c. The transverse velocity and shear stress are spurious results related to the node distribution within the horizon.

An additional grid effect evident in these simulations is the influence of mesh spacing orthogonal to the wave propagation. The velocity and stress are approximately 5–10% higher in the fine grid region on the left than in the coarse mesh region on the right. The grid is uniform on the left and right of the body, so this lateral node spacing effect is independent of the grid gradient effects.

The second calculation with the same graded mesh examines the potential complementary shear-volume coupling. In this simulation, all of the nodes are constrained in the vertical and out-of-plane directions. A 50-mm/ms transverse velocity boundary condition is imposed on the bottom and top 1 mm of material. The center 1 mm of material is given a -50 -mm/ms transverse velocity. This creates two 1-mm thick regions subjected to simple shear boundary conditions similar to plugging. The imposed x -direction velocity field is shown in figure 13.

The resulting out-of-plane stress and dilatation are shown in figures 14a and 14b, respectively. The deformation causes dilatation and a corresponding out-of-plane stress, even though the deformation is nominally isochoric in the regions between the applied velocities, and all nodal velocities in the other two directions are set to zero. There are significant stresses in the vertical and horizontal directions, but these are primarily due to rotation of the stress tensor, and the magnitude is not attributed to kinematic coupling. The out-of-plane stress in figure 14a should be unaffected by the stress tensor rotation. The dilatation and the out-of-plane stress are not consistent with the boundary conditions and material constitutive response.

It should be noted that the stress and dilatation are less in the uniform grid regions (but not adjacent to the edges where boundary effects play a role). This supports the assertion that these artifacts are created by the graded grid and would not occur if the grid were uniform.

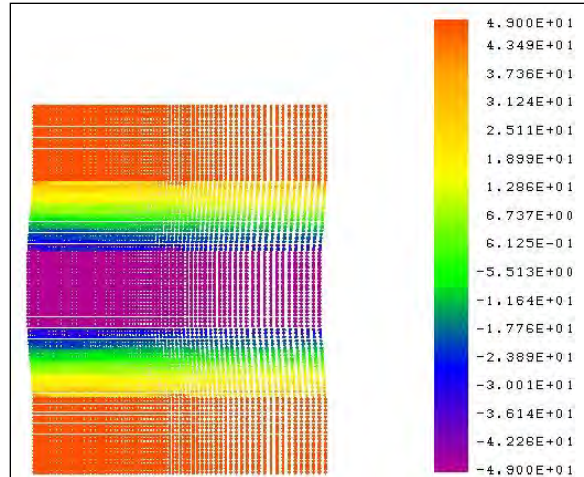


Figure 13. Horizontal velocity field (m/s) creating two simple shear regions. The solid color regions at the top, center and bottom are nodes where the velocity is imposed.

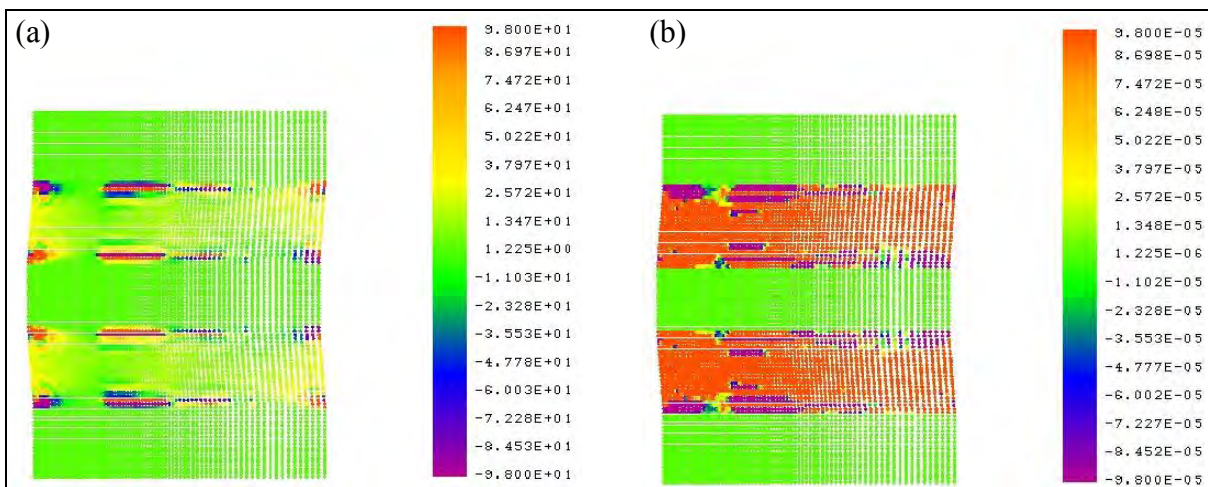


Figure 14. The (a) out of plane stress (MPa) and (b) dilatation resulting from imposed simple shear boundary conditions on the graded mesh.

3.2.5 Impact with a Spherical Projectile

The sphere impact calculation of section 3.1.4 is repeated with ductile and brittle state-based materials. A 30-mm square target, 20 mm deep with a 0.5-mm grid spacing, was impacted by a dense, rigid 10-mm diameter sphere traveling at 200 mm/ms. The target had a density of 0.0022 g/mm^3 , a Young's modulus of 70 GPa, a Poisson's ratio of 0.28, and a yield strength of 1300 MPa. The failure strain was set to 100 for the ductile material and to 0.01 for the brittle material.

The dilatation for the ductile target is shown in figure 15 at approximately 0.034 ms after impact. At this time, the penetration depth is over 6 mm—deeper than the penetrator radius. Due to the high failure strain, the damage is insignificant, on the order of $1.e-6$. There are two important observations from this image. First is that the surface heaving does not appear consistent with the volume of material displaced by the impactor (the vertical displacement on the sides is nearly zero). Given the low surface displacement, considerable densification would be expected, as in figure 7b. However, the levels indicated are much lower. The second observation is that the node locations and dilatation values under the penetrator are in disarray; some dilatation values even indicate expansion. Together, these observations suggest a breakdown in the ductile calculation at these very large deformations.

The dilatation plots for the sphere impacting the brittle material at approximately 0.034 ms are shown in figure 16. The dilatation value is set to zero upon material failure. As with the ductile calculation, there appears to be insufficient surface displacement to accommodate the volume of the impactor. The nodes appear significantly compressed beneath the impactor and are likely constrained by the short-range interactions, since the specified constitutive relations would not apply for failed material. The region immediately below the sphere is punched vertically, and there are large velocity discontinuities associated with the fractures on either side plug.

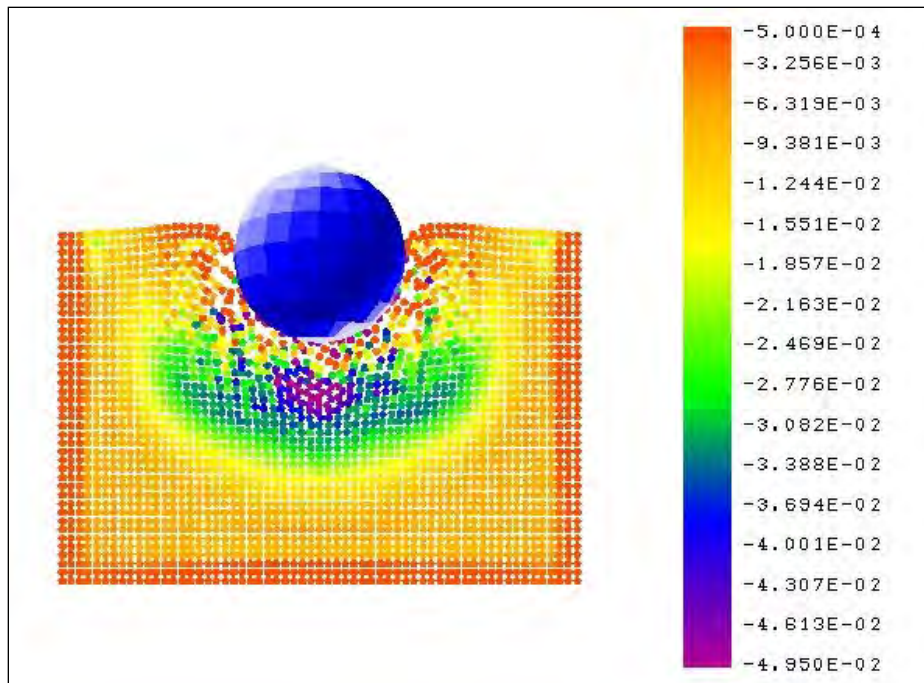


Figure 15. Dilatation plot for a dense, rigid sphere impacting a ductile target. The disordered nodes and color levels combined with an apparent densification suggest a breakdown of the calculation. The initial configuration is shown in figure 7a.

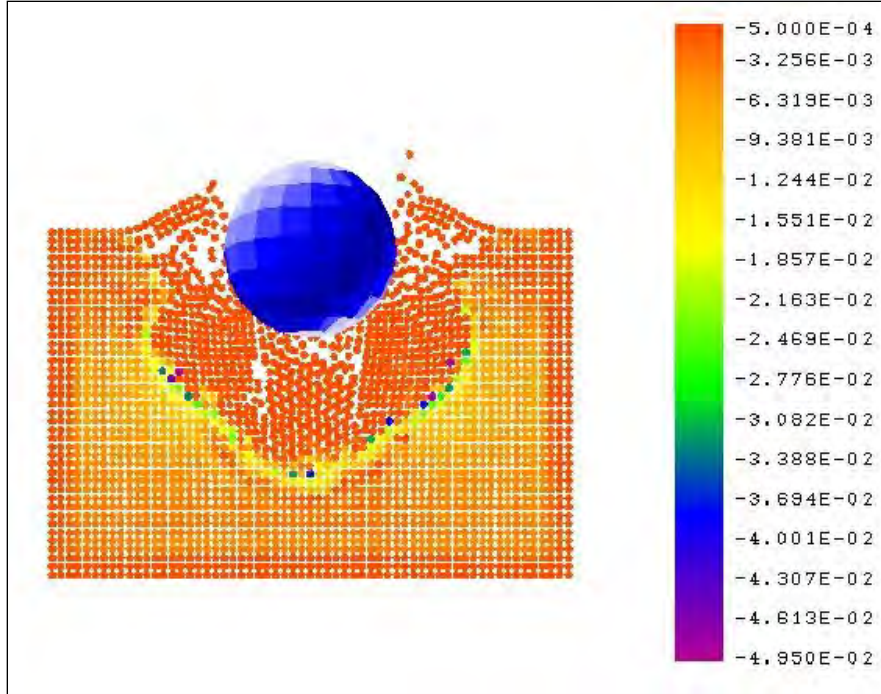


Figure 16. Dilatation plot for a dense, rigid sphere impacting a brittle target. The tight node packing suggests that the hydrodynamic response is being controlled by the short-range interaction force rather than the constitutive response.

4. Kinematics of the State-based Formulation

The results from EMU show volume-shear coupling when using both a shifted grid (figure 4) and a spatially graded grid (figure 12). Such couplings are inconsistent with the governing equations. It is instructive to investigate the behaviors to determine whether they result from the kinematics, the momentum balance, or some numerical aspect. The kinematic description is analyzed in this section through both analytic solutions and simplified numerical results.

4.1 Analytic Solutions

4.1.1 Normal impact with a Shifted Grid

The volume-shear coupling in a shifted grid is examined by considering the 2D sheared mesh in figure 17. The vertical spacing of the horizontal lines of nodes is one unit, and the nodes are one unit apart along the horizontal lines. Each successive row of nodes is shifted by 0.2 units to the right from the row below it. A horizon of 2.3 units is used to keep the problem easily tractable. To simulate the initial stages of longitudinal wave propagation, a velocity is assumed on the bottom row of nodes and the remainder of the nodes is still at rest.

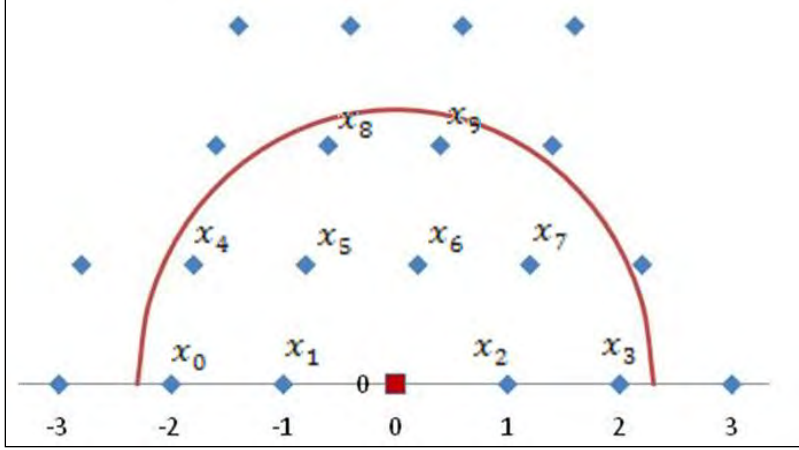


Figure 17. Shifted 2D grid used to investigate volume-shear coupling.

The ξ values for the labeled nodes are calculated as

$$\begin{aligned} \xi_0 &= (-2, 0); & \xi_1 &= (-1, 0); & \xi_2 &= (1, 0); & \xi_3 &= (2, 0); & \xi_4 &= (-1.8, 1); \\ \xi_5 &= (-0.8, 1); & \xi_6 &= (0.2, 1); & \xi_7 &= (1.2, 1); & \xi_8 &= (-0.6, 2); & \xi_9 &= (0.4, 2). \end{aligned} \quad (13)$$

These are combined to create the \mathbf{K} tensor, as in equation 4, assuming that the node volumes are one and the weighting function is one within the horizon. The components of \mathbf{K} and \mathbf{K}^{-1} are

$$K_{ij} = \sum_{n=0}^9 (\xi_n \otimes \xi_n)_{ij} = \begin{bmatrix} 15.88 & -1.6 \\ -1.6 & 12 \end{bmatrix} \quad \text{and} \quad K_{ij}^{-1} = \frac{1}{188} \begin{bmatrix} 12 & 1.6 \\ 1.6 & 15.88 \end{bmatrix}. \quad (14)$$

Assume a vertical velocity on the first row of $\bar{\mathbf{V}}$; let \mathbf{v}_n be the velocity vector of the nodes and let \mathbf{v}_x be the velocity vector of the focus node. The Cartesian components of the velocity gradient are

$$L_{ij} = \sum_{n=0}^9 [(\mathbf{v}_n - \mathbf{v}_x) \otimes \xi_n]_{il} K_{lj}^{-1} = \frac{\bar{V}}{188} \begin{bmatrix} 0 & 0 \\ 1.4 & -8 \end{bmatrix} \begin{bmatrix} 12 & 1.6 \\ 1.6 & 15.88 \end{bmatrix} = \frac{\bar{V}}{188} \begin{bmatrix} 0 & 0 \\ 4 & -124.8 \end{bmatrix}. \quad (15)$$

The non-zero 21 component of the velocity gradient indicates a shear strain rate, which creates a shear stress. The 22 component of the velocity gradient would be equal to the velocity divided by the grid spacing in a local algorithm, but it is low by almost 34%. The nonlocal nature of the formulation encompasses additional nodes and spreads the displacement over a wider area. It is interesting to note that if nodes 8 and 9 are omitted from the calculations, the shear is zero and the error in the 22 component of the velocity gradient is also zero. Removing these points removes much of the nonlocal influence for this configuration, and it resembles a local model.

With the exception of a regular grid and a normal velocity, it is not obvious how to discern which node arrangements will produce a shear deformation and which will not. In the shifted grid example, the shear deformation is dependent on the magnitude of the shift and the horizon. To illustrate this point, consider the horizon of 2.3 units in the previous example. If the nodal

shift per row is less than 0.06789 of the grid spacing, the shear will be zero. A horizon of 2.5 times the grid spacing allows for a grid shift per row of 0.25 of the grid spacing without shear error. The reason for this is the number and symmetry of nodes entering or leaving the horizon.

4.1.2 Point-wise Solution on Irregular Grid

The effect of a node shift perpendicular to the wave can potentially be offset by shifts on other nodes. A mesh that appears severely distorted may not necessarily produce a shear deformation at every point. For example, consider the grid in figure 18.

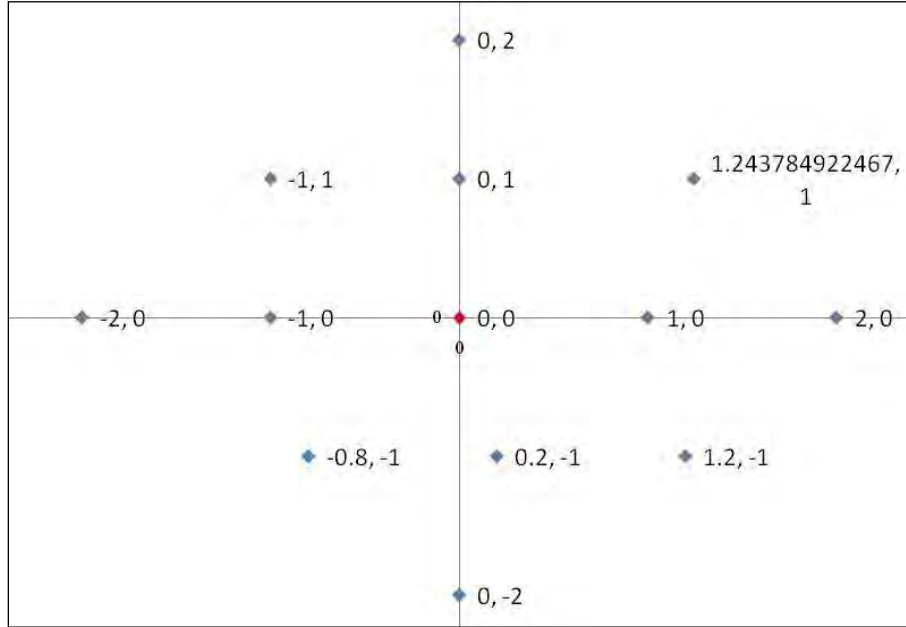


Figure 18. Grid with single point shifted to create a zero shear error at a specific node.

The mesh in figure 18 has an origin at (0,0) and a horizon of 2.2 units; all 13 digits are significant for this example. A boundary condition forces nodes on and below the x -axis to have constant velocity in the y -direction. Here the nodal volume, V_n , is calculated as

$$V_n = (x_n - x_0)^2 + (y_n - y_0)^2. \quad (16)$$

The shape tensor is calculated as

$$\mathbf{K} = \sum_{n=1}^{12} (\xi_n \otimes \xi_n) * V_n = \begin{bmatrix} 14.7589408826158 & 0.717704414172386 \\ 0.717704414172386 & 14.0594310884222 \end{bmatrix}, \quad (17)$$

and the inverse is

$$\mathbf{K}^{-1} = \frac{1}{206.987212651112} * \begin{bmatrix} 14.0594310884222 & -0.717704414172386 \\ -0.717704414172386 & 14.7589408826158 \end{bmatrix}. \quad (18)$$

Letting \bar{V} be the y -direction velocity of the nodes below the x -axis yields a velocity gradient at the origin of

$$\mathbf{L} = \bar{V} \begin{bmatrix} 0 & 0 \\ 7.43849426498855 * 10^{-16} & 0.359860299936931 \end{bmatrix} . \quad (19)$$

This illustrates that the shear deformation for this mesh at this point is zeroed by judicious placement of a single node. This adjustment, however, likely adds to the shear at adjacent nodes.

Two points can be gleaned from this example. First, the only way to be certain of the kinematic coupling that an irregular grid will generate in peridynamics is to calculate it. There is no obvious pattern or rule of thumb. Second, artifacts introduced by an irregular grid can vary from point to point and need not be smooth.

4.1.3 Horizon Effect and Discretization Error

The discretization error in computing the deformation gradient can be estimated for simple configurations. Suppose a 1-D string of nodes is stretched such that the new position of the nodes is governed by the quadratic relation

$$x = X + X^2\alpha . \quad (20)$$

Here α is a constant, x is the new position vector, and X is the original position vector. The 1D deformation gradient is equal to the derivative of the displaced coordinate with respect to the initial coordinate. For this problem, the deformation gradient at any point equals

$$\frac{dx}{dX} = 1 + 2\alpha X . \quad (21)$$

According to the above equation, the deformation gradient at the origin ($X = x = 0$) should be equal to 1. Assuming a horizon of 3, the nonlocal shape tensor is 28 and the deformation vector state is 28. This gives a deformation tensor of exactly 1 at the origin. In fact, any horizon used with this equation and a uniform grid will give the exact result at all nodes.

Next, consider a higher order displacement where the new positions are governed by the cubic equation

$$x = X + X^3\alpha . \quad (22)$$

For this displacement field, the deformation gradient at any point should be equal to

$$\frac{dx}{dX} = 1 + 3\alpha X^2 . \quad (23)$$

The deformation gradient at the origin ($X = x = 0$) should again be equal to 1. With a horizon of 3, the nonlocal shape tensor is 28, but the deformation vector state is now $28 + 196\alpha$; this gives a deformation gradient of $1 + 7\alpha d^2$, where d is the node spacing. For any non-zero value of α , the deformation gradient has an error. This result is compared to the same problem with a

different horizon. Assuming a horizon of 2.9 times the grid spacing, the deformation gradient is $1 + 3.4\alpha d^2$, and for a horizon of 1.1, the deformation gradient is $1 + \alpha d^2$. This indicates that the error in the deformation gradient is dependent on the chosen horizon as well as the grid spacing. It is not difficult to show that the error for the cubic displacement field is

$$Error = \alpha d^2 \frac{\sum_{n=1}^H n^4}{\sum_{n=1}^H n^2}, \quad (24)$$

where H is the number of nodes included in the horizon to either side of the node of interest. Following this trend, the error is reduced as the horizon is decreased. When the horizon is reduced to a single node spacing, a local model rather than a nonlocal model, the 1D peridynamics solution resembles the finite difference method.

4.2 Numerical Evaluation

The analytic results illustrate the effect of nodal placement on the calculation of the velocity gradient using the state-based formulation. These solutions are for individual points and do not give an overall picture of the distribution of the volume-shear coupling. To provide a larger scale evaluation, a stand-alone, 2D code was written to calculate the deformation gradient using the relations given by Foster, et al. (7). The initial and displaced coordinates are specified for all points, and the only aspect of the state-based peridynamics solution being evaluated is the calculation of the deformation gradient.

4.2.1 Volume-shear Coupling

The stand-alone calculations were used to investigate the volume-shear coupling for several mesh configurations: sinusoidal, graded, and rotated (figure 19). In all cases, the same displacement field is applied. The initial and final x -coordinates are identical. The displaced y -coordinates of the upper portion of the grid are the same as the initial coordinates, so the deformation gradient is the identity tensor in the upper region. The coordinates in the lower portion of the grid are shifted up 10% of the average grid spacing, and the deformation gradient for this rigidly displaced region is also the identity. The deformation gradient is nonuniform in the transition region. The transition follows a hyperbolic tangent function of the form

$$y = Y + (0.1 d) \frac{1}{2} \left[1 - \tanh \left\{ 2 \left(\frac{Y - 10d}{d} \right) \right\} \right], \quad (25)$$

where Y is the initial coordinate, y is the displaced coordinate, and d is the grid spacing. The grid spacing was 0.3 mm in the y -direction, and the mesh height was approximately 16 mm.

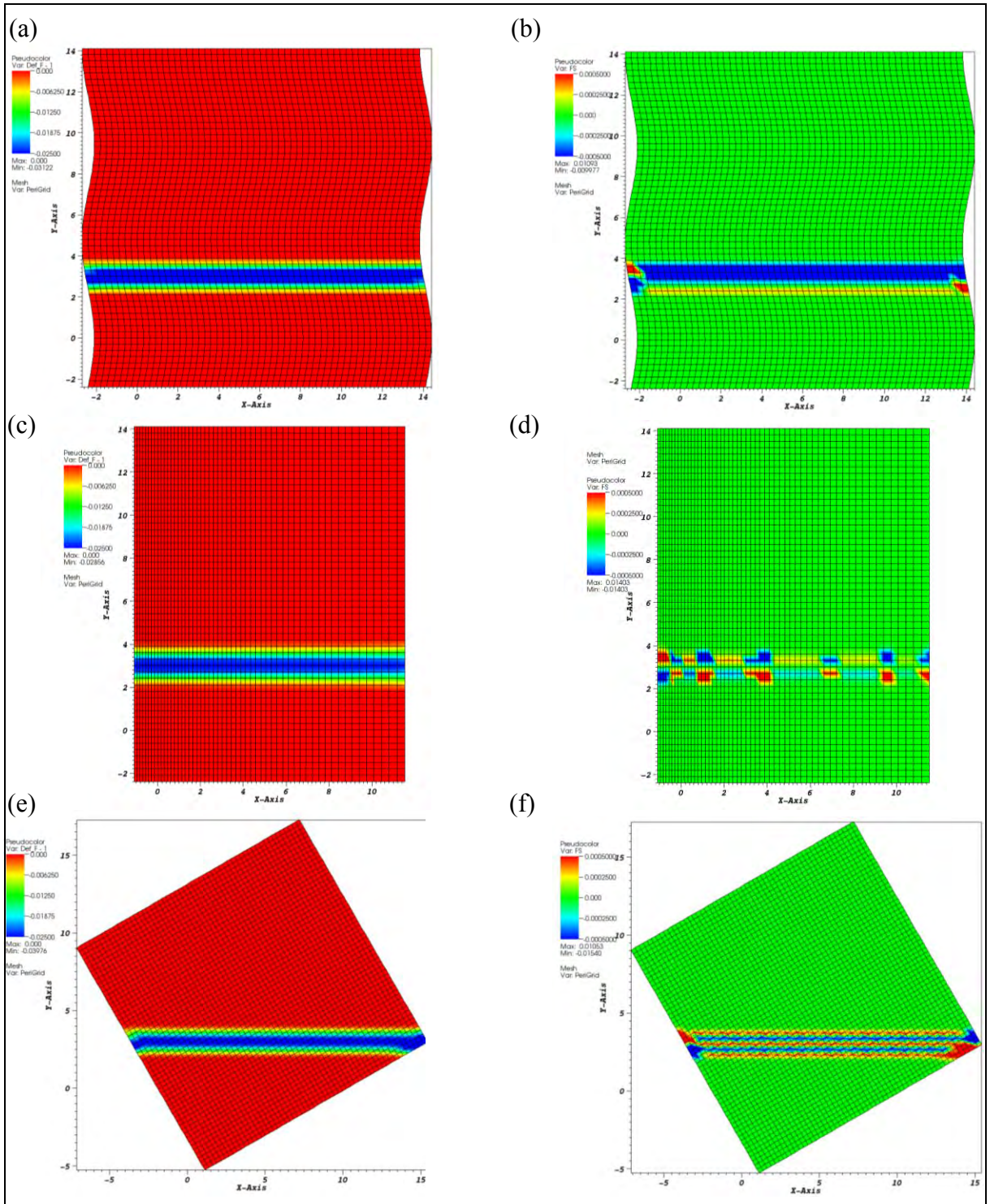


Figure 19. Grid configurations illustrating volume-shear coupling. (a), (c) and (e) show the volume change imposed on the grid. Plots (b), (d) and (f) illustrate the corresponding shear induced by the volume change.

The results are shown in figure 19. The left column shows the grid and the volume change ($\text{Det } F - 1$). The corresponding plots at the right show the shear induced by this volume change. The shear induced in the sinusoidal mesh, shown in figures 19a and 19b, is anticipated because EMU

had already shown that a sheared mesh will induce the coupling. The coupling for the graded mesh, shown in figures 19c and 19d, was also observed in EMU, but figure 19d shows additional localized high shear spots that correspond to points dropping into and out of the horizon. The last results in figure 19 are for a rotated mesh. Here the sharp gradient induces pattern of positive and negative shear.

These grids were also run as a wave propagation calculation in EMU. Some degree of volume-shear coupling was observed in all. The shear shown by EMU for the sinusoidal mesh strengthens and weakens as the mesh curvature changes. Volume-shear coupling is observed at early times for the rotated mesh, but as the wave front spreads over several grid spacings, the shear fades into the noise. The graded mesh calculations in EMU were presented earlier.

It is important to remark that a linear displacement field (affine deformation) gives no shear for any of the grids shown in figure 19. This is consistent with the proof accompanying equation 13 in Foster, et al. (7). In addition, the shear contribution is zero if the nodes are set on a regular orthogonal grid aligned with the wave propagation.

An additional feature to note in figure 19 is that the shear deformation is highest at the boundaries, where the nodes are asymmetric within the horizon.

4.2.2 Horizon Effects in a Collapsing Cylinder

The second assessment of the peridynamic state-based deformation gradient calculation was on a regular orthogonal grid, since most of the grid effects discussed thus far are greatly diminished for a regular orthogonal grid. The closed form analysis in section 4.1.3 suggests sensitivity of the solution to the displacement gradient and to how points are included in the horizon, so these aspects are investigated numerically.

The problem considered is the isochoric, radial collapse of a cylinder. The analytic solution is simple, and the inhomogeneous deformation samples the grid at every angle. The cylinder has a 20-mm outside radius and a 10-mm inside radius (A), and it is deformed modestly so that the inside radius is displaced to a radius of 9 mm (a). The regular grid spacing chosen was 0.3 mm. The deformed coordinates of all nodes were prescribed consistent with an isochoric radial collapse. The coordinates remain on a radial line with original radius R and the deformed radius given by

$$r = \sqrt{R^2 - A^2 + a^2} , \quad (26)$$

which is based on area calculations and is valid to arbitrarily large strains. While only a 1/4 segment of the cylinder is shown, a larger portion of the cylinder was analyzed to eliminate edge effects on the x and y symmetry axes.

Results are shown in figure 20 for progressively larger horizons that envelop an additional node in rows and columns adjacent to the evaluated node. The horizons are 1.015, 1.5, 2.015, 2.3, 3.015, and 3.2 times the grid spacing. The quantity plotted is the volume change ($\text{Det } F - 1$), which should be zero for the given isochoric deformation. The existence of discretization error is

not unexpected, although the magnitude is of some concern. The pressure error within the cylinder would be a significant fraction of the flow stress for a typical metal.

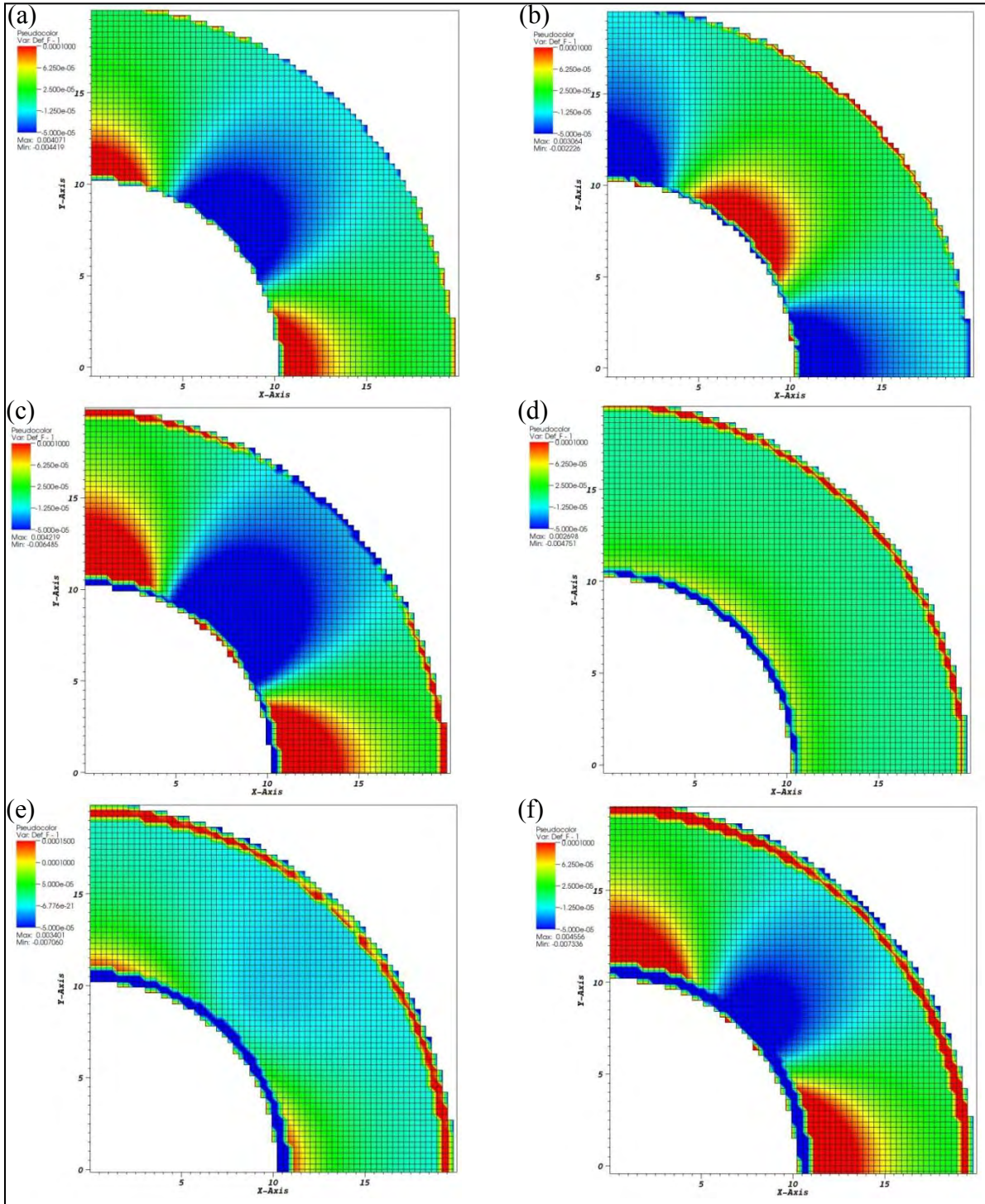


Figure 20. Calculated volume change resulting from nodal displacements corresponding to an isochoric deformation field. The horizon for the plots is: (a) 1.015, (b) 1.5, (c) 2.015, (d) 2.3, (e) 3.015, and (f) 3.2 times the grid spacing. The color levels are the same for each plot.

What is interesting in figure 20 is how the patterns and magnitude of the error shift as the horizon changes to include more points. The changes occur in steps, so a point moving into or out of the horizon would cause a step change in pressure. Also significant is the large volume change at the inner and outer radii. Here, the volume strain can exceed half a percent; it occurs abruptly in transition from the interior to the boundary regions; and multiple transitions occur in the boundary region.

5. Discussion

One of the frequently cited features of peridynamics is that it replaces partial differential equations of conventional continuum theory with integral equations (1, 8, 9). However, when the peridynamic and FE strain calculations are viewed side by side at comparable stages of their formulations, this distinction is not apparent. Both involve integrals over volumes. The cited distinction of integral versus differential equations is a result of comparing different aspects of the formulations.

The integrands for the two methods do differ. The conventional continuum methods use analytic derivatives, and peridynamics uses a difference approximation to the derivative. At a small enough point spacing, the difference approximations to gradients can also resemble singularities. As an example, this construct can be taken to the smallest sensible level—the atomic spacing. If the material points are taken to correspond to atomic positions with initial spacing on the order of 2.5×10^{-4} microns, a 100-micron-wide crack would have a stretch of 4×10^5 ; this is not the infinite stretch associated with a crack in a traditional continuum framework, but it is still large enough to dominate the behavior of the integral.

This distinction in gradient representation becomes academic when the equations are discretized through nodal relations. The deformation gradient and velocity gradient are formed from sums and differences among nodal coordinates and velocities. The manner in which the nodal values are combined can vary considerably for the two methods, and, as a nonlocal method, peridynamics includes significantly more nodes in the strain calculations. Consequently, the results can be quite different.

The nodal force calculations in peridynamics are significantly different from FE nodal force calculations. The momentum balance in peridynamics uses a difference between stress vector states at neighboring nodes. This resembles the strong form of the momentum equations, whereas FE typically uses a weak form.

Another cited attribute of peridynamics is that the fracture occurs naturally on bonds connecting nodes rather than through additional equations, stress intensity factors, and prescribed crack paths that must be imposed in conventional continuum formulations (1). This comparison is to special techniques used in simulations where detailed crack stress fields are resolved, rather than

the more broadly used FE failure methods. The failure criteria in peridynamics are quite similar to simple FE failure models used in large-scale hydrocodes. The peridynamics micro models use bond stretch to trigger failure, and the state-based models use a critical strain to initiate failure. A strain to failure is one of the simpler failure criteria applied in FE analyses.

Material failure in peridynamics is progressive and should exhibit less grid sensitivity than the abrupt failure that is often used in finite elements. Detailed comparison of peridynamics fracture and FE failure using nonlocal constitutive relations or progressive stress release algorithms is needed.

The post-failure tensile response of peridynamics allows unrestrained separation of nodes on either side of the fracture surface. Lagrangian FE allows a similar unhindered separation, although element deletion may be necessary to prevent numerical issues when there are large displacements between the two surfaces.

Material densification in peridynamics following compressive failure is controlled by the short-range interaction forces. These forces result from separate equations, not the constitutive relations. It is possible to have unhindered compression between the time of fracture and the activation of the short-range force. This unhindered compression is primarily responsible for the unrealistic densification seen in the impact simulations. In conventional Lagrangian, FE the pressure-volume relation within an element is still enforced following failure if the pressure is positive. In these cases, conversion of failed material to smooth particle hydrodynamics (SPH) particles (12) can be used to provide continuous repulsive forces at large deformations. It should be possible to modify peridynamics to use the equation of state so that a separate short-range interaction force is not necessary. It might also be possible to modify the short-range forces in peridynamics to achieve a continuous compression response.

As links between nodes are removed due to failure, the distribution of nodes within the horizon contributing to the solution will change. It was demonstrated previously, e.g., figure 20, that such changes to the node distribution can induce step changes in nodal strain fields, even if the node is not immediately adjacent to the fracture. The volume and/or shear deformation can experience jump discontinuities when nodes are added to or removed from the horizon. The discontinuous nature of the mesh effects makes it difficult to identify and quantify errors. The magnitude and effect of such jumps on the details of the stress and strain fields during failure should be examined to determine whether or not the crack propagation solution is affected significantly.

An additional aspect of failure to consider is the fracture surface. The nonlocal formulation introduces boundary effects that will be present on these newly created free surfaces. Figures 8, 14, 19, and 20 all show effects associated with surfaces. In figure 8, the surface nodes and the nodes 3 rows from the surface have nearly identical displacement histories for a wave transit problem. This is not expected from the governing equations. In figures 14 and 19, the edges have larger volume-shear coupling than the interior, and in figure 20, an artificial volume change of

more than 0.5% was calculated at the boundary for the isochoric displacement field. There is no reason to expect that these surface effects would not also be present at crack surfaces.

In light of the combination of nonlocal effects at free surfaces and effects from links broken within the horizon, the accuracy of the stress and strain solutions near a crack should be examined in detail. The crack tip displacement, strain, and stress fields should be compared to analytic solutions to determine the extent to which the nonlocal formulation and numerical discretization impact the results. This is beyond the scope of the current study.

Difficulties associated with boundary conditions in nonlocal methods may also be important for other surfaces and interfaces. If the strain or stress state is perturbed significantly at a surface, evaluation of the failure criteria at the surface could also be affected. Alternatively, if two surfaces impact and the contact is only made at the surfaces nodes, the impact conditions may not be imposed properly. In order to create the expected surface behaviors, it may be necessary to refine the grid sufficiently to reduce the spatial extent of the perturbations or to develop special boundary conditions consistent with the numerical treatment, as is done in finite difference implementations (13), certain hydro codes (e.g., CTH [14]), and other nonlocal methods, such as Element Free Galerkin (15).

Many results were presented illustrating grid-dependent volume-shear coupling for irregular and non-orthogonal grids. The effects result from a combination of the nonlocal method and asymmetries of the node distribution within the horizon. Such effects are not consistent with the governing equations and will introduce unanticipated shear and pressure into the results. One possible way around these effects may be to only use regularly spaced orthogonal grids. These appear to avoid the most severe volume-shear coupling. However, there is still some coupling for inhomogeneous deformation fields, as illustrated by the collapsing cylinder; and it is not possible to create conformal boundaries on arbitrary geometries using regular grids. Further detailed evaluations are necessary to determine conditions under which peridynamics will produce accurate general deformation results, including strain and stress states at boundaries and interfaces.

Dissipation is a significant aspect of the peridynamic solution in the context of wave propagation. Stress waves often set the loading for high-rate fracture simulations, so wave propagation can be quite important. The nonlocal nature of the strain and momentum calculations averages the fields within the horizon. The horizons from adjacent nodes have significant overlap and this overlap can propagate information to neighboring nodes. This was illustrated by the effect of horizon on rise time seen in comparing figures 2a and 3a. Dispersion is also evidenced by the variation in wave propagation speed, where the lower particle velocity moves faster through the material than the higher particle velocity. This velocity difference leads to further spreading of the wave front. Additional dissipation comes from application of drag forces to quiet noise in the solution. The drag algorithm ties all nodes within a family, thereby

suppressing peak values and further diminishing gradients, as shown in figure 9. It has a much broader effect than control of zero-energy modes.

The long-range interactions in peridynamics necessitate many equations for each node. A typical concern for techniques where the equations greatly outnumber the degrees of freedom is that solutions will be over-constrained. This will occur if there is inconsistency among the constraints arising either from the underlying equations or the numerical approximation. The possibility that over-constraint is responsible for the unexpected velocity patterns in figure 8a and the node locations in figure 15 should be investigated.

A final discussion topic concerns solution accuracy in relation to the number of points in the horizon. The relative position vector, ξ , is numerically larger for nodes closer to the horizon than for nodes near the center of the integration region. Multiplying the differences in field quantities by the relative position vector effectively gives a greater weight to values from more distant nodes. Concurrently, including the distant nodes increases the magnitude of the shape tensor. Dividing by the larger shape tensor also reduces the influence of the nodes adjacent to the node of interest. The combined result is that accuracy can be diminished significantly as the horizon is increased, as illustrated in section 4.1.3. Thus, it would seem that the most accurate solutions would be obtained by only including adjacent nodes. This would result in a local model, and the discretized peridynamics equations would resemble the well-known finite difference relations. Alternatively, the weighting function could be employed to ensure that more distant nodes have progressively less impact, as in element free Galerkin methods (15). This is another area for future study.

6. Conclusions and Recommendations

A side-by-side comparison of deformation gradient calculations for peridynamics and finite elements suggests that the oft-cited distinction of integral equations versus differential equations is likely an impression from comparing different aspects of the formulations—both methods use integrals over volumes, but the integrands use different approximations. The greatest distinction is that peridynamics is a nonlocal method, whereas traditional finite elements is a local method.

A survey of the peridynamics solutions for pre- and post-fracture mechanical deformation was undertaken using a combination of analytic methods and the EMU and KRAKEN codes from Sandia. The study revealed anomalous behaviors related to the numerical grid, the nonlocal formulation, and the particular model implementations.

The nonlocal method and grid effects can produce artifacts that are not consistent with the governing equations:

- Volumetric and shear deformations are coupled through the kinematics if the node distribution within the horizon is irregular. A volume change can induce shear deformation, and a shear deformation can induce a volume change.
- The solution can deviate considerably from expectation on boundaries because nonlocal boundaries have a finite thickness of several node spacings. Fracture surfaces are also boundaries and may be impacted by nonlocal effects.
- There is high dispersion of field quantities, most notably, significant spreading of wave solutions.

There are also features related to the particular implementation and material models used. These result from implementation choices and should be relatively straight-forward to improve.

- When the micro-elastic and micro-plastic models are stressed beyond the yield point the results are not consistent with the physical behavior of materials. The pressure-volume response also follows the plasticity relation and the effective bulk modulus is softened.
- Compression response of state-based materials at large deformation and following fracture is governed by the short-range interaction force rather than the equation of state.
- The drag algorithm controlling zero-energy modes is applied broadly as a smoothing function rather than explicitly constraining only hourglass modes. Specific zero-energy modes are not identified.
- Solution errors can grow significantly as the integration horizon is increased.

Given the current modeling capabilities of EMU and KRAKEN, potential application for the peridynamics codes are brittle tensile fracture for the micro-elastic models and more general tensile fracture for the state-based models. Even for these applications, analysts should understand how the problem set-up and results may differ from more conventional approaches, and ensure that the behaviors are consistent with expectations, particularly at boundaries. Algorithm modification and extensive, detailed validation of deformation and stress fields would be needed for applications involving fracture and compression, particularly for large strains associated with high-speed impact simulations.

As with any new computational tool, the analyst should run numerous detailed comparisons with existing solutions, analytic methods, and data on the class of problems of interest to verify that the results are correct and that the new method has quantifiable advantages. The benefits of potentially less mesh sensitive fracture have to be balanced against grid sensitivities, boundary effects, and limited constitutive behaviors.

7. References

1. Silling, S. A. Reformulation of Elasticity Theory for Discontinuities and Long-Range Forces. *J. Mech. Physics Solids* **2000**, *48*, 175–209.
2. Silling, S. A.; Epton, M.; Weckner, O.; Xu, J.; Askari, E. Peridynamics States and Constitutive Modeling. *J. Elast.* **2007**, *88*, 151–184.
3. Demmie, P. N.; Silling, S. A. An Approach to Modeling Extreme Loading of Structures Using Peridynamics. *J. Mech. Mater. Struct.* **2007**, *2*, 1921–1945.
4. Doh, H. Y.; Bobaru, F. Studies of Dynamic Crack Propagation and Crack Branching with Peridynamics. *Int. J. Fract.* **2010**, *162*, 229–244.
5. Silling, S. A.; Weckner, O.; Askari, E.; Bobaru, F. Crack Nucleation in a Peridynamic Solid. *Int. J. Fract.* **2010**, *162*, 219–227.
6. Kilic, B.; Agwai, A.; Madenci, E. Peridynamic Theory for Progressive Damage Prediction in Center-Cracked Composite Laminates. *Composite Struct.* **2009**, *90*, 141–151.
7. Foster, J. T.; Silling, S. A.; Chen, W. W. Viscoplasticity Using Peridynamics. *Int. J. Num. Meth. Engrg.* **2009**, *81*, 1242–1258.
8. Silling S.; Cole R.; Demmie P.; Foster J.; Taylor P. *EMU User's Manual Version 2.6.38*; Sandia National Laboratories: Albuquerque, NM, 2011.
9. Demmie, P. N. *Kraken User's Manual Version 1.0*. 2011, Sandia National Laboratories, Albuquerque, NM.
10. Flanagan, D. P.; Belytschko, T. A Uniform Strain Hexahedron and Quadrilateral with Orthogonal Hourglass Control. *Int. J. Numer. Meth. Engrg.* **1981**, *17*, 679–706.
11. Silling, S. A. Private Communication. August 16, 2011.
12. Johnson, G. R. Numerical Algorithms and Material Models for High-Velocity Impact Computations. *Int. J. Impact Eng.* **2011**, *38*, 456–472.
13. Gerald, C. F. *Applied Numerical Analysis*; Addison-Wesley Publishing Co, 1978.
14. Crawford, D.A.; Brundage, A. L.; Harstad, E. N.; Hertel, E. S. Jr.; Schmitt, R. G.; Schumacher, S. C.; Simmons, J. S. *CTH User's Manual and Input Instructions Version 10.0*; Sandia National Laboratories: Albuquerque, NM, 2011.
15. Dispersion Analysis and Element-Free Galerkin Solutions of Second and Fourth-Order Gradient-Enhanced Damage Models. *Int. J. Numer. Meth. Eng.*, **2000**, *49*, 811–832.

NO. OF COPIES	ORGANIZATION	NO. OF COPIES	ORGANIZATION
1 ELEC	ADMNSTR DEFNS TECHL INFO CTR ATTN DTIC OCP 8725 JOHN J KINGMAN RD STE 0944 FT BELVOIR VA 22060-6218	2	NAVSEA DAHLGREN ATTN C DYKA ATTN M HOPSON 6138 NORC AVE STE 313 DAHLGREN VA 22448-5157
3	SANDIA NATL LABS ATTN MS 0836 S SCHUMACHER ATTN MS 0380 K MISH ATTN MS 0836 E HARSTAD PO BOX 5800 1515 EUBANK SE ALBUQUERQUE NM 87185-0836	1	LOS ALAMOS NATL LAB ATTN E MAS PO BOX 1663 LOS ALAMOS NM 87545
4	US ARMY ARDEC ATTN RDAR MEE W C CHIN ATTN RDAR MEE W D PFAU ATTN RDAR MEE W G STUNZENAS ATTN RDAR MEE W E BAKER BLDG 3022 PICATINNY ARSENAL NJ 07806-5000	5	RICHARD J LUCAS 5161A CLEARBROOK DRIVE OXFORD MS 38655
3	US ARMY ARDEC ATTN RDAR MEF E D CARLUCCI ATTN RDAR MEF E D GEISSLER ATTN RDAR MEF E S RECCHIA BLDG 94 PICATINNY ARSENAL NJ 07806-5000	1	U.S. ARMY RSRCH LAB ATTN RDRL WMP B S SATAPATHY ABERDEEN PROVING GROUND MD 21005
1	LAWRENCE LIVERMORE NATL LAB ATTN L-140 D FAUX PO BOX 808 LIVERMORE CA 94550	1	US ARMY RSRCH LAB ATTN RDRL CIH C D GROVE ABERDEEN PROVING GROUND MD 21005
1	LIVERMORE NATL LAB ATTN L-098 ROSE MCCALLEN PO BOX 808 LIVERMORE CA 94551	20	US ARMY RSRCH LAB ATTN RDRL CIH C J CAZAMIAS ATTN RDRL WML J NEWILL ATTN RDRL WMP B A DARGO ATTN RDRL WMP B C HOPPEL ATTN RDRL WMP B D POWELL ATTN RDRL WMP B J CLAYTON ATTN RDRL WMP B M RAFTENBERG ATTN RDRL WMP B M SCHEIDLER ATTN RDRL WMP B R BECKER (10 HCS) ATTN RDRL WMP B S BILYK ATTN RDRL WMP C T W BJERKE BLDG 390 ABERDEEN PROVING GROUND MD 21005
3	SANDIA NATL LABS ATTN MS 1322 D LITTLEWOOD ATTN MS 1322 S SILLING ATTN MS-1165 P DEMMIE PO BOX 5800 ALBUQUERQUE NM 87185-5800	2	US ARMY RSRCH LAB ATTN RDRL CIH C J KNAP ATTN RDRL CIH C P CHUNG BLDG 310E ABERDEEN PROVING GROUND MD 21005
1	UNIV OF MISSISSIPPI DEPT OF MECH ENGRG ATTN A M RAJENDRAN 201 B CARRIER HALL UNIVERSITY MS 38677		

NO. OF COPIES	ORGANIZATION	NO. OF COPIES	ORGANIZATION
1	US ARMY RSRCH LAB ATTN RDRL WML B B RICE ABERDEEN PROVING GROUND MD 21005	1	US ARMY RSRCH LAB ATTN RDRL WMP B R KRAFT ABERDEEN PROVING GROUND MD 21005
2	US ARMY RSRCH LAB ATTN RDRL WMM B C RANDOW ATTN RDRL WMM B G GAZONAS ABERDEEN PROVING GROUND MD 21005	4	US ARMY RSRCH LAB ATTN RDRL WMP D B VONK ATTN RDRL WMP D D KLEPONIS ATTN RDRL WMP D G VUNNI ATTN RDRL WMP D H W MEYER ABERDEEN PROVING GROUND MD 21005
5	US ARMY RSRCH LAB ATTN RDRL WML M J ZOLTOSKI ATTN RDRL WMM B B CHEESEMAN ATTN RDRL WMM B R WILDMAN ATTN RDRL WM B FORCH ATTN RDRL WM J MCCAULEY BLDG 4600 ABERDEEN PROVING GROUND MD 21005	1	US ARMY RSRCH LAB ATTN RDRL WMP E B CHAMISH ABERDEEN PROVING GROUND MD 21005
1	US ARMY RSRCH LAB ATTN RDRL WMM G J ANDZELM BLDG 4600 RM C204 ABERDEEN PROVING GROUND MD 21005	2	US ARMY RSRCH LAB ATTN RDRL WMP E C NICELY ATTN RDRL WMP H C MEYER ABERDEEN PROVING GROUND MD 21005
4	US ARMY RSRCH LAB ATTN RDRL WMM J BEATTY ATTN RDRL WMM J ZABINSKI ATTN RDRL WMM R DOWDING ATTN RDRL WMP A B RINGERS ABERDEEN PROVING GROUND MD 21005	5	US ARMY RSRCH LAB ATTN RDRL WML H M FERREN-COKER ATTN RDRL WML H S SCHRAML ATTN RDRL WMP P J BAKER ATTN RDRL WMP S E SCHOENFELD ATTN RDRL WMP G S KUKUCK BLDG 309 ABERDEEN PROVING GROUND MD 21005
4	US ARMY RSRCH LAB ATTN RDRL WMP B B LEAVY ATTN RDRL WMP D J RUNYEON ATTN RDRL WMP D R DONEY ATTN RDRL WMP E B LOVE BLDG 393 ABERDEEN PROVING GROUND MD 21005	4	US ARMY RSRCH LAB ATTN RDRL D OFFICE OF DIRECTOR ATTN IMNE ALC HRR MAIL & RECORDS MGMT ATTN RDRL CIO LL TECHL LIB ATTN RDRL CIO MT TECHL PUB ADELPHI MD 20783-1197
1	US ARMY RSRCH LAB ATTN RDRL WMP B J HOUSKAMP ABERDEEN PROVING GROUND MD 21005		